

THE TEMPERATURE STRUCTURE OF 30 NEARBY CLUSTERS OBSERVED WITH ASCA. SIMILARITY OF TEMPERATURE PROFILES

MAXIM MARKEVITCH^{1,3}, WILLIAM R. FORMAN¹, CRAIG L. SARAZIN², AND ALEXEY VIKHLININ^{1,3}

ApJ in press; astro-ph/9711289

ABSTRACT

We present an analysis of ASCA spatially resolved spectroscopic data for a nearly complete sample of bright clusters with redshifts between 0.04 and 0.09. Together with several clusters analyzed elsewhere using the same method, this sample consists of 30 objects with $T_e \gtrsim 3.5$ keV for which we obtained projected temperature profiles and, when possible, crude two-dimensional temperature maps. The clusters are A85, A119, A399, A401, A478, A644, A754, A780, A1650, A1651, A1795, A2029, A2065, A2142, A2256, A2319, A2597, A2657, A3112, A3266, A3376, A3391, A3395, A3558, A3571, A3667, A4059, Cygnus A, MKW3S, and Triangulum Australis. All clusters, with the possible exception of a few with insufficiently accurate data, are found to be nonisothermal with spatial temperature variations (apart from cooling flows) by a factor of 1.3–2. ASCA temperature maps for many clusters reveal merger shocks. The most notable of these are A754, A2065, A3558, A3667, and Cygnus A; merging can also be inferred with lower confidence from the A85, A119, and A2657 temperature maps and from the A3395 and Triangulum Australis entropy maps. About half of the sample shows signs of merging; in about 60% of the sample, we detect cooling flows. Nearly all clusters show a significant radial temperature decline at large radii. For a typical 7 keV cluster, the observed temperature decline between 1 and 6 X-ray core radii (0.15 and $0.9 h^{-1}$ Mpc) can be approximately quantified by a polytropic index of 1.2–1.3. Assuming such a polytropic temperature profile and hydrostatic equilibrium, the gravitating mass within 1 and within 6 core radii is approximately 1.35 and 0.7 times the isothermal β -model estimates, respectively.

Most interestingly, we find that temperature profiles, excluding those for the most asymmetric clusters, appear remarkably similar when the temperature is plotted against radius in units of the estimated virial radius. We compare the composite temperature profile to a host of published hydrodynamic simulations. The observed profiles appear steeper than predictions of most Lagrangian simulations (Evrard, Metzler, & Navarro 1996; Eke, Navarro, & Frenk 1997). The predictions for $\Omega = 1$ cosmological models are most discrepant, while models with low Ω are closer to our data. We note, however, that at least one $\Omega = 1$ Lagrangian simulation (Katz & White 1993) and the recent high-resolution Eulerian simulation (Bryan & Norman 1997) produced clusters with temperature profiles similar to or steeper than those observed. Our results thus provide a new constraint for adjusting numerical simulations and, potentially, discriminating among models of cluster formation.

Subject headings: Cosmology — galaxies: clusters: individual — intergalactic medium — X-rays: galaxies

1. INTRODUCTION

It has been twenty years since the realization that the extended X-ray emission from clusters (e.g., Kellogg et al. 1972) is thermal and arises from optically thin plasma filling the clusters (e.g., Mitchell et al. 1976). This plasma is in hydrostatic equilibrium in most clusters and delineates the distribution of the cluster gravitational potential. If one could measure the spatial distributions of the density and temperature of this plasma, it is possible to calculate the distribution of total cluster mass, including its dominant dark matter component (e.g., Bahcall & Sarazin 1977; Mathews 1978). Such measurements have cosmological implications. Most importantly, the observed high fraction of hot gas in the total cluster mass is a strong argument for a low value of the cosmological density parameter Ω_0 (e.g., White et al. 1993). The spatial distribution of the cluster plasma temperature is interesting in itself, because it is an indicator of the cluster dynamical state. Hydrodynamic simulations show that clusters which recently formed via mergers of smaller subunits should have a complex temperature structure which becomes more regular with time (e.g., Schindler & Müller 1993; Roettiger, Burns, & Loken 1993). Determination of the dy-

namical state of present-day clusters can constrain cosmological models, because rich clusters should be dynamically older in an open universe than in a high-density universe (White & Rees 1978; Richstone, Loeb, & Turner 1992). Although recent simulations (e.g., Thomas et al. 1997) suggest that the degree of irregularity of the cluster images is not as strongly dependent on Ω_0 as it was thought, temperature maps contain additional information on the cluster dynamics that may enable more sensitive tests. The spatial distribution of cluster temperatures also may provide clues on the significance of nongravitational sources of gas thermal energy, such as supernovae-driven galactic winds (e.g., Metzler & Evrard 1997).

The most promising quantitative approach to these interesting problems is to compare the observed cluster temperature and density structure with predictions of cosmological hydrodynamic simulations. Presently, independent simulation techniques seem to converge on the same qualitative results for cluster dark matter and gas distributions within the framework of their assumed physical models (e.g., Frenk et al. 1998), although their resolution is still insufficient to model the fine details of the gas density distribution. In some sense, the op-

¹Harvard-Smithsonian Center for Astrophysics, 60 Garden St., Cambridge, MA 02138; maxim, wrf, alexey @head-cfa.harvard.edu

²Department of Astronomy, University of Virginia, Charlottesville, VA 22903; cls71@virginia.edu

³Also Space Research Institute, Russian Academy of Sciences

posite holds for present-day observations — while the X-ray imaging instruments such as *Einstein* and *ROSAT* have obtained high-resolution gas density maps for a large number of clusters, until recently, detailed spatially resolved temperature data were unavailable. The early X-ray spectroscopic instruments lacked imaging capability, while imaging instruments had limited spectral resolution or bandwidth. Coarse spatial temperature distributions were obtained only for the nearest clusters such as Coma, Perseus, and Virgo with *EXOSAT* (Hughes, Gorenstein, & Fabricant 1988), *Spacelab-2* (Eyles et al. 1991; Watt et al. 1992), and *Ginga* (Koyama, Takano, & Tawara 1991). The *ROSAT* PSPC was the first instrument to combine good spatial and adequate spectral resolution for energies below 2 keV. It obtained temperature distributions for several galaxy groups and cool clusters (e.g., Ponman & Bertram 1993; David, Jones, & Forman 1995). The *ROSAT* temperature maps for several hot clusters were published as well (e.g., Briel & Henry 1994, 1996; Henry & Briel 1995, 1996), but see Markevitch & Vikhlinin (1997a, hereafter MV97a) for a more realistic estimate of their uncertainties.

The *ASCA* X-ray observatory (Tanaka, Inoue, & Holt 1994) is capable of measuring the temperature distributions in nearby clusters. The *ASCA* energy band (0.5–11 keV) is well-suited for clusters, and the 3' half-power diameter angular resolution is adequate. Although analysis of the *ASCA* data is complicated by the mirror effects such as the energy dependence of the point spread function (Takahashi et al. 1995) and sometimes stray light (Ishisaki 1996), there are published results on cluster temperature structure that take these effects into account. Markevitch et al. (1994, 1996a) presented results for A2163. The analysis method presented in the latter paper was used for several other published cluster temperature maps (see references in Table 1 below) and is used in this paper. Applying independent techniques, Ikebe et al. (1996, 1997) analyzed the Fornax and Hydra A clusters. Loewenstein (1997) reported preliminary results on A2218; Honda et al. (1996) presented a temperature map of Coma, while Ezawa et al. (1997) reported on the temperature and abundance profile of AWM7. A temperature map of A1367 has been obtained by Donnelly et al. (1997), and a more detailed map of the central part of Coma by Jones et al. (1997)

In this paper, we report on the first systematic study of a representative sample of 30 nearby hot clusters, which we have undertaken to determine the common properties of their spatial temperature distributions. Because of the statistical purpose of this investigation, we give only a brief description of individual clusters, some of which will be discussed in more detail in subsequent papers. We concentrate on the cluster-scale temperature structure and only perform the necessary minimum of modeling of such details as cooling flows, point sources in the field, etc. For these components, we allow maximum parameter freedom to obtain model-independent measurements for the main cluster gas. We use $H_0 = 100 h \text{ km s}^{-1} \text{ Mpc}^{-1}$ and $q_0 = 0.5$.

2. THE SAMPLE

We selected clusters in the redshift interval $0.04 \leq z \leq 0.09$ with 0.1–2.4 keV fluxes greater than about $2 \times 10^{-11} \text{ erg s}^{-1} \text{ cm}^{-2}$ from the *ROSAT* All Sky Survey X-ray-bright Abell cluster sample (Ebeling et al. 1996), and included Cygnus A, MKW3S and Triangulum Australis missing from the Abell catalog due to Galactic obscuration. The redshift range is chosen so that the most distant clusters of the sample are

still well resolved by *ASCA*, while for the most nearby clusters, radii of interest ($0.5 - 1 h^{-1} \text{ Mpc}$) and the bright cluster cores are covered by the single *ASCA* field of view, so that stray light contamination from outside the field of view of the observation (Ishisaki 1996) does not complicate the analysis. The redshift and flux selection results in 35 clusters; we analyze 30 of them that currently have accessible *ASCA* data (see Table 1). For our present purposes, it is unimportant that the sample is not a complete flux-limited one. Rather, we aim at a representative sample of clusters with a range of temperature and having different evolutionary stages. Our list includes such diverse clusters as A754 which is undergoing a major merger (e.g., Henry & Briel 1995) as well as A1795 and A2029 which are among the most regular X-ray and strongest cooling flow clusters (e.g., Buote & Tsai 1996). The sample includes clusters with average temperatures from 4 to 10 keV, with mergers and strong cooling flows at both ends of the temperature interval. In addition to the variety of X-ray morphologies, A780 (Hydra A) and Cygnus A are examples of clusters with powerful central radio sources, while A3558 is located in the dense environment of the Shapley Supercluster.

3. METHOD

The *ASCA* mirrors have an energy-dependent point spread function (PSF) with an average half-power diameter of 3' (Serlemitsos et al. 1995). The PSF effects should be taken into account when deriving spatially resolved temperature distributions (e.g., Takahashi et al. 1995). The method for doing this, which we use here, is described in Markevitch et al. (1996a) and Markevitch (1996, hereafter M96). Here we present its brief outline and relevant additional details. In this paper, we study spatial distributions of projected cluster gas temperatures. For this, we divide each cluster image into regions, usually selected to coincide with interesting surface brightness features, and assume that the spectrum is uniform over each region. Because *ASCA* has insufficient angular resolution to obtain, simultaneously, both surface brightness and temperature distributions with sufficient accuracy for clusters in our sample, we use higher-resolution images from the *ROSAT* PSPC for all clusters except A1650 and A2065, for which *Einstein* IPC and IPC combined with *ROSAT* HRI were used, respectively. These images are used as models of the surface brightness distributions which determine relative normalizations between the projected emission measures in different cluster regions.

ASCA spectral data are collected from the regions in the detector plane that correspond to the sky regions, applying the SIS and GIS field of view boundaries. Direct and scattered flux contributions from each sky region to each detector region are calculated by multiplying the model image by the *ASCA* effective area and convolving it with the *ASCA* PSF (both dependent on position and energy) for each energy bin, then integrating the result over the respective detector regions. Then cluster temperatures in all model regions are fitted simultaneously to the spectra from all regions, all detectors, and all pointings if there is more than one.

3.1. Brightness Model from *ROSAT* PSPC

We used the Snowden et al. (1994) code to generate *ROSAT* PSPC images in the 0.5–2 keV energy band (or in the 0.9–2 keV band for clusters with the highest Galactic absorption to maximize the signal to noise ratio). An X-ray background was determined for each cluster individually by fitting the outer radii of

TABLE 1
CLUSTER SAMPLE

Name	Exposure, ks ^c		z	T_e single-comp. ^a keV	T_X weighted ^b keV	r_{180} arcmin ^c	Ref.	Notes ^d
	GIS	SIS						
A85	27+14	21+10	0.052	6.1 ± 0.2	6.9 ± 0.4	38.9		m, CF
A119	32	18	0.044	5.8 ± 0.6	5.6 ± 0.3	40.6		m
A399	29+38	22+31	0.072	7.4 ± 0.7	7.0 ± 0.4	29.2		
A401	32+38	27+31	0.074	8.3 ± 0.5	8.0 ± 0.4	30.6		
A478	33	15	0.088	7.1 ± 0.4	8.4 ^{+0.8} _{-1.4}	26.9		CF
A644	52	45	0.071	7.1 ± 0.6	7.9 ± 0.8	31.5	1	m, CF?
A754	21	16	0.054	9.0 ± 0.5	9.5 ^{+0.7} _{-0.4}	44.0	2	M
A780 (Hydra A)	26	23	0.057	3.8 ± 0.2	4.3 ± 0.4	28.5		CF
A1650	49	42	0.085	5.6 ± 0.6	6.7 ± 0.8	24.9		CF
A1651	32	25	0.085	6.3 ± 0.5	6.1 ± 0.4	23.7		
A1736	17	...	0.046	3.5 ± 0.4		
A1795	36	28	0.062	6.0 ± 0.3	7.8 ± 1.0	35.2		CF
A2029	34	30	0.077	8.7 ± 0.3	9.1 ± 1.0	31.6	3	CF
A2065	23+23	20+21	0.072	5.4 ± 0.3	5.5 ± 0.4	25.9	4	M, CF
A2142	14+17	9+14	0.089	8.8 ± 0.6	9.7 ^{+1.5} _{-1.1}	28.6		CF
A2256	28+35	21+24	0.058	7.5 ± 0.4	6.6 ± 0.4 ^f	34.4	5	
A2319	13+15	10+12	0.056	9.2 ± 0.7	8.8 ± 0.5	41.4	6	
A2597	39	30	0.085	3.6 ± 0.2	4.4 ^{+0.4} _{-0.7}	20.0		CF
A2657	45	32	0.040	3.7 ± 0.3	3.7 ± 0.3	36.3		m, CF
A3112	34	15	0.070	4.7 ± 0.4	5.3 ^{+0.7} _{-1.0}	26.0		CF
A3266	33	24	0.055	7.7 ± 0.8	8.0 ± 0.5	40.2		
A3376	21	...	0.046	4.3 ± 0.6	4.0 ± 0.4	32.9		
A3391	21	14	0.054	5.7 ± 0.7	5.4 ± 0.6	33.5		γ
A3395	31	22	0.050	4.8 ± 0.4	5.0 ± 0.3	34.6		m
A3558	17	12	0.048	5.5 ± 0.3	5.5 ± 0.4	37.6	7	M, CF, γ ?
A3571	23+19+22	15+15+19	0.040	6.9 ± 0.3	6.9 ± 0.2	50.0		CF
A3667	16	13	0.053	7.0 ± 0.6	7.0 ± 0.6	38.5	4	M, CF
A4059	36	26	0.048	4.1 ± 0.3	4.4 ± 0.3	33.5		CF
Cygnus A	29+33	24+25	0.057	6.5 ± 0.6	6.1 ± 0.4	33.7	4	M, γ
MKW3S	30	24	0.045	3.5 ± 0.2	3.7 ± 0.2	32.6		CF
Triangulum	11+7	9+4	0.051	9.5 ± 0.7	9.6 ± 0.6	46.8	8	m; γ or CF?

^a Single-temperature fit to the spectrum of the whole cluster. Errors are 90%

^b Emission-weighted gas temperature excluding cooling flow and other contaminating components, see §5

^c Estimated from T_X , see §6

^d Detected in our temperature data: CF — significant central cool component; γ — central power-law component; M — major merger; m — some indication of merging

^e Entries with “+” are exposures for multiple pointings

^f Including secondary cluster. Excluding secondary, 7.3 ± 0.5 keV.

References: 1—Bauer & Sarazin (1998); 2—map presented in Henriksen & Markevitch (1996); 3—Sarazin et al. (1997); 4—maps in M98; 5—M96, MV97b; 6—map in M96; 7—MV97a; 8—map in MSI.

the PSPC field of view by a constant plus a power law cluster radial brightness profile. All clusters in our sample are sufficiently small so that separating the outer cluster halo and the background did not pose a problem. The *ROSAT* band X-ray background averaged over areas similar in size to the regions of our temperature maps ($\sim 10'$ in diameter) has an rms scatter of about 10%, while the background averaged over larger areas similar to the outer bins of our radial temperature profiles ($\sim 30-40'$) has a scatter of 5% (Vikhlinin & Forman 1995; Soltan et al. 1996). These estimates of the PSPC background uncertainty are included in our confidence intervals.

There is an ambiguity in defining a background when a significant fraction of it is resolved into point sources. Hard point sources that are bright in the *ASCA* band were fitted individually along with the surrounding cluster temperatures, to account for their scattered flux. Softer sources that are bright only in the *ROSAT* band were excluded from the fit by masking them from the model and detector regions. Otherwise, they may lead to an overestimate of the emission measure in the outer, low surface brightness regions of the cluster, resulting in a slightly lower best-fit *ASCA* temperature. Given the limited *ASCA* resolution, it is not practical to excise all point sources detectable

in the *ROSAT* image, therefore the integral contribution of the remaining numerous weak sources should be subtracted as part of the background. We have calculated the *ROSAT* background consistently with this requirement, by excluding from the background calculation region only sources as bright as those excluded from the *ASCA* fitting region.

3.2. *ASCA* PSF Model and Choice of Energy Band

Above 2 keV, the *ASCA* PSF is modeled by interpolating between the Cyg X-1 GIS images at different focal plane positions (Takahashi et al. 1995; Ueno 1996). At lower energies, Cyg X-1 appears intrinsically extended and is inadequate for PSF modeling. In this work, we use *ASCA* data in the 1.5–11 keV band, excluding the 2–2.5 keV interval with a poorly calibrated effective area, and extrapolate the PSF model from higher energies to the 1.5–2 keV interval (assuming a higher PSF uncertainty of 10%). We have chosen to include the latter interval despite the increasing PSF uncertainty in order to take advantage of the high statistical precision data below the 2.2 keV mirror reflectivity edge. Another reason for including it is that for many clusters, we found that discarding lower energy data resulted in slightly higher (by about 0.5 keV) temperatures. This can be expected given that the effective area calibration is more accurate over the whole *ASCA* energy band than in any smaller interval. Even though this difference is smaller than most individual temperature uncertainties, we tried to avoid such a bias. For a check, we analyzed all observations with the energy cut-off at 1.5 and 2.5 keV and found no significant differences in best-fit temperature values except for that mentioned above.

For modeling of the SIS data, the GIS Cyg X-1 calibration images were corrected for the energy dependence of the intrinsic GIS detector blurring by additional smoothing resulting in a final constant resolution (Gaussian $\sigma = 0.5'$). The cluster SIS data also were smoothed to the same resolution.

3.3. Treatment of Cooling Flows

In this work, cluster cooling flows are considered “contaminants” whose effect on the measured temperatures of the main cluster gas should be removed. Usually we can confidently detect the presence of an additional spectral component at the center of a cooling flow cluster, but in most cases we cannot say whether it is a cooling flow, an additional lower single-temperature, or a power law component without a detailed analysis (e.g., of spectral lines and the surface brightness) which is beyond the scope of this work. The best-fit temperatures in the outer cluster regions are essentially independent of these details, as long as our chosen model describes the central spectrum adequately and the relative normalization of the central and the outer regions is correct.

Due to the spectral complexity of cooling flows, the relative emission measure of the central cluster region calculated from the *ROSAT* PSPC image (as is done for other regions) is inadequate. For this reason and to allow maximum model independence, we fitted, as free parameters, the normalization of the central region relative to other regions, the fraction of a cooling flow (or another spectral component) in the total emission from that model region, and the temperature of its main thermal component, from which the cooling was assumed to start. A cooling flow spectrum was modeled as prescribed in Sarazin & Graney (1991). Because of the large number of free parameters for the central spectra and the PSF uncertainty associated with the small regions ($r = 1.5'$ or $2'$) used to model cooling flows,

the derived central temperatures for strong cooling flow clusters are weakly constrained. Generally, the cooling flow model parameters are not usefully constrained and therefore are not presented.

Bright point sources that are seen both in *ROSAT* and *ASCA* images were fitted following the same procedure.

3.4. Data and Model Coordinate Alignment

It is important that the model image, derived from *ROSAT* or *Einstein*, is accurately aligned with the *ASCA* image. A small offset can result in an error of the model flux in the regions surrounding the brightness peak that is greater than the statistical uncertainty, especially for clusters with strong cooling flows. The standard *ASCA* 1σ coordinate accuracy of $24''$ (Gottlieb 1996) is insufficient for this purpose. Therefore, we corrected the *ASCA-ROSAT* coordinate offset for each individual observation by comparing the *ROSAT* image (convolved with the *ASCA* PSF) to the actual *ASCA* image. The uncertainty of such corrections is $6\text{--}13''$ (1σ), depending on how peaked the cluster is.

In the course of this work we also have noticed a systematic $0.4'$ offset between the GIS and SIS detector coordinates. For the same reason as above, this offset can result in an inconsistency between the GIS and SIS temperature maps of cooling flow clusters. We corrected this offset; our previous papers did not consider strong cooling flows and therefore were not significantly affected.

3.5. *ASCA* Data Filtering and Background Calculation

We have applied a conservative version of the standard filtering criteria to the *ASCA* data (ABC Guide <http://heasarc.gsfc.nasa.gov/docs/asca/abc/abc.html>). In addition, SIS data that showed telemetry saturation were excluded. The resulting exposures (averages of two SISs and two GISs) are presented in Table 1. For the GIS, we used only the data within $18'$ of the detector centers, and corrected the detector gain maps for their long-term time dependence (Makishima 1996). For the SIS, we analyzed faint and bright mode data and different clocking modes together. Our results are insensitive to the time dependence of the SIS spectral resolution, and a 1.5 keV energy cutoff ensures that they are also insensitive to the uncertainty of the SIS efficiency at the energies below ~ 0.8 keV (e.g., Sarazin, Wise, & Markevitch 1997).

For the background calculation, we used *ASCA* observations of blank fields. For the SIS, the normalization was calculated using the total useful exposure, applying a correction for the long-term mode-dependent degradation of the SIS efficiency (Dotani et al. 1995) since the background fields were observed early in the mission. A 1σ uncertainty of 20% was assumed for the SIS background normalization.

For the GIS, the blank field data were normalized by exposures in the individual cut-off rigidity intervals as a first approximation. For the smaller and fainter clusters in our sample, it was possible to model and subtract the cluster emission from the same GIS image in the hard energy band (where the cluster is faint and at the same time the background is most important), and normalize the blank field background to the residual. An uncertainty of such normalization was 5–7% (1σ). The normalization determined in such a way showed good agreement with that determined from the exposure values, with a typical deviation of less than 10%. We therefore assumed a 10% 1σ un-

certainty for bright clusters for which such a direct background estimate was impossible.

3.6. Summary of Systematic Uncertainties

To summarize, the following systematic uncertainties (1σ) were included in our temperature confidence intervals in addition to the statistical uncertainties:

GIS and SIS background normalization errors of 5–20%;

An *ASCA* effective area calibration uncertainty of 5% of the model flux in each energy interval (this incorporates the uncertainty of the mirror optical axis positions, see Gendreau & Yaqoob 1997);

A PSF error of 10% for radial temperature profiles, of 10% for temperature maps in the PSF core for relatively small regions (e.g., cooling flows), and of 15% for temperature maps in the wings of the PSF;

A *ROSAT* surface brightness model error, including the *ROSAT* statistical error and background uncertainties of 5% for the temperature profiles and 10% for the temperature maps;

A 6–20'' relative *ASCA-ROSAT* image offset uncertainty.

Effects of the PSF, effective area and *ASCA* background uncertainties on the spatially-resolved temperature values obviously are reduced when the cluster is observed in several offset pointings, ideally with different telescope roll angles, because possible spatially dependent miscalibrations then average out. Ten clusters in the sample have multiple pointings, of them A2256, A3571 and Cygnus A have been observed with different roll angles. Use of all four *ASCA* detectors also reduces the effects of PSF and effective area errors, since the mirror optical axes are offset by a few arcminutes with respect to each other.

The PSF scattering seriously complicates our measurements. In the outermost radial bins of our clusters, only 30–60% of the flux at an energy of 5 keV originates in the corresponding region in the sky, while the remaining flux is that scattered from the bright inner cluster regions. We will see below that for the distant cooling flow clusters that have sharp central brightness peaks and therefore the greatest scattered fraction, the PSF uncertainty translates into large uncertainties in the outer temperatures. This usually precludes the reconstruction of accurate two-dimensional temperature maps.

3.7. Fitting Procedure

The GIS and SIS spectra from each detector (SIS chips were treated as independent detectors) were binned in several (5–13) intervals with different width so that χ^2 minimization could be performed. To avoid finding false minima of χ^2 as a function of many free parameters, we used the annealing minimization technique (e.g., Press et al. 1992). The Raymond & Smith (1977, 1992 version) model for thermal emission was used. In most cases, abundances in different regions were not usefully constrained and therefore were fixed at the cluster average values. Given the *ASCA* spectral resolution, this practically does not affect the obtained best-fit temperature values.

Generally, we used spectra from all detectors for each region to reduce systematic uncertainties. We excluded from the fit the spectra with insufficient statistics, for example, due to the partial coverage when a given region is better covered by another pointing, or due to the SIS small field of view when the GIS has sufficient data for this region. When fitting the temperature maps, we also excluded SIS spectra for regions with small partial chip coverage to avoid problems due to the possi-

ble temperature nonuniformity inside each region. Normalizations between different detectors were free parameters, while relative normalizations between different model regions were fixed or freed as described above. Due to our rather conservative inclusion of systematic uncertainties, values of χ^2_{\min} per degree of freedom were less than 1 in all fits. One-parameter confidence intervals for the fitted parameters were estimated by Monte-Carlo simulations that included all statistical and systematic uncertainties.

For a consistency check, we fitted GIS and SIS data separately, finding reasonable agreement in all cases but two. For A3376, we were unable to obtain consistent results from GIS and SIS, most likely due to the anomalous SIS background in that observation, and chose to use only the GIS data. For A1736, we obtained unacceptable χ^2 values for all SIS fits and for GIS spatially-resolved fits, again possibly for the background reasons. This cluster only has a relatively low-quality IPC image which did not allow a more accurate GIS background normalization as described in §3.5. Therefore, for A1736, we only present a wide-beam GIS temperature which should not be significantly affected by this uncertainty.

For those clusters with more than one pointing, we also performed separate fits for different pointings for another consistency check. The results were consistent within their expected errors, confirming the adequacy of the adopted systematic error estimates.

4. RESULTS

4.1. Wide-beam Temperatures

To check the consistency between our results and earlier wide-beam measurements, we have performed single-temperature fitting of the overall cluster spectra (for $r < 16-18'$) without exclusion of point sources (except for Cygnus A which was fit by a thermal plus an absorbed power law component) or use of cooling flow models. GIS and SIS data were fitted simultaneously, except that SIS data were not used when it was observing in 1-CCD mode with a field of view of only $11' \times 11'$ (A644, A1650, A2657, A3266, A3391, Triangulum Australis). Absorption columns were fixed at their Galactic values taken from Dickey & Lockman (1990). The resulting temperature values are given in Table 1. Fig. 1 shows these values compared to those from David et al. (1993), who presented wide-beam *Einstein* MPC results and compiled the most accurate *EXOSAT* (Edge & Stewart 1991) and *Ginga* (Hatsukade 1989) measurements. We added a later Cygnus A *Ginga* result from Ueno et al. (1994). Only those David et al. values with an accuracy of better than 50% are shown. For several clusters where MPC and either *EXOSAT* or *Ginga* disagreed, both measurements are shown.

The figure shows that over the whole range of temperatures in the sample, our temperatures are in good agreement with previous measurements. The most notable exceptions, marked by circles, merit explanation. The highest-temperature deviation is Triangulum Australis, whose *EXOSAT* temperature is lower than ours. Markevitch, Sarazin, & Irwin (1996b, hereafter MSI) showed that most of this discrepancy is caused by different assumed N_H values (Edge & Stewart obtained a best-fit N_H value higher than Galactic; however, *ROSAT* PSPC observations yielded a value very close to the Galactic value which we use). Also, an update of the GIS gain calibration (Makishima 1996) has resulted in a slightly lower *ASCA* temperature than the one reported in MSI. Further, our 7.7 keV temperature for

A3266 is inconsistent with the lower MPC value. A soft point source seen in the *ROSAT* PSPC image just outside our fitting region (see Fig. 2) may contribute to this discrepancy. Our 6.0 keV value for A1795 is higher than the *Ginga* value but agrees with the MPC value (the MPC and *Ginga* values are themselves discrepant). This cluster has a strong cooling flow and instruments with different energy coverage are likely to obtain different single-temperature fits. As expected, our single-temperature fit for A1795 depends on the adopted low energy cutoff. The energy band difference between *ASCA* and the MPC may also be the reason of the A2065 discrepancy. For this cluster, we obtain $T = 5.4$ keV but also detect large spatial temperature variations probably due to a merger (Markevitch et al. 1998, hereafter M98). The separate GIS and SIS single-temperature fits are similar, and it is noteworthy that our A2065 temperature is in a better agreement with the $L_X - T$ relation (David et al. 1993) than the higher MPC value.

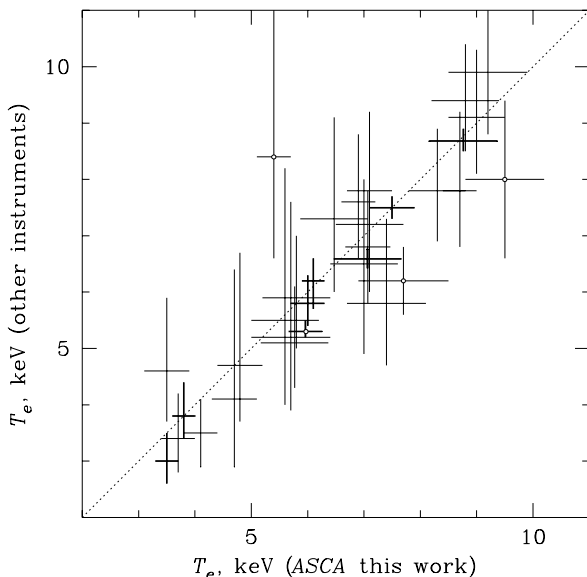


FIG. 1.—Comparison of our temperatures with those from *Einstein* MPC, *EXOSAT* and *Ginga* (David et al. 1993; Ueno et al. 1994). Errors are 90%. Values from more than one earlier instrument are shown if they disagreed. Bold crosses denote the most accurate of the David et al. values. Circles denote the most notable discrepancies, discussed in text.

Having performed this consistency check, we show below that single-temperature values often have little meaning, because clusters are nonisothermal and many have strong cooling flow contributions.

4.2. Temperature Maps and Radial Profiles

Figures 2 and 3 present two-dimensional temperature maps for 9 clusters with superposed *ROSAT* PSPC brightness contour maps. We show only clusters for which the temperature maps have useful accuracy. Temperature maps obtained for A644, A754, A2029, A2065, A2256, A2319, A3558, A3667, Cygnus A, and Triangulum Australis are published separately (see references in Table 1). In Figs. 2 and 3, we tried to assign different shades of gray to significantly different temperatures, but it was not always possible due to the very different confidence intervals. Individual clusters are discussed in the section below.

Figure 4 shows radial projected temperature profiles for all clusters in our sample except for A644, A2029, A2256, A2319, and A3558 published elsewhere (see references in Table 1), A2597 which is dominated by a cooling flow (see below), and A1736 for which we do not have a profile (see §3.7). The profiles were obtained in the annuli around the centroid of the large-scale emission, which did not always coincide with the brightness peak (an extreme example is the double cluster A3395, see Fig. 3). Generally, we did not exclude from the radial profiles any substructures (except for the contaminating point sources) even when they were obvious, in order to be able to compare these results to the future low statistics data on distant clusters.

4.3. Results for Individual Clusters

A85.—A temperature map is reconstructed in the annuli $r = 0 - 1.5' - 6' - 12' - 20'$, with the second and third annuli divided into 4 equal sectors and the outermost annulus in two unequal sectors (Fig. 2). Sectors 6 and 10 coincide with an infalling subcluster (e.g., Durret et al. 1997). In the center, we detect a strong cooling flow. The normalization of this spectral component is greater than zero at greater than 99.9% confidence. A single-temperature fit is shown in the map and the upper temperature of a cooling flow is shown in the radial profile in Fig. 4. The temperature declines with radius, and the map shows no highly significant deviations from azimuthal symmetry. However, if the less massive infalling subcluster were only a projection, the correspondent sectors would appear cooler than adjacent regions (as, for example, in A2256 or A2319, M96). Instead, the map and the profile (Fig. 4) show that the subcluster regions are probably hotter than the adjacent ones, suggesting the presence of shock-heated gas arising from an ongoing collision. A more detailed temperature map, e.g., from *AXAF*, should detect such shocks.

A119.—The temperature map is reconstructed on a grid of $6' \times 6'$ boxes, with regions 1 and 2 composed of 2 boxes and region 15 of 4 boxes for better accuracy. Region 10, coincident with one of the infalling or projected subclusters seen both in the X-ray image and in the optical data (Way, Quintana, & Infante 1997), is significantly cooler than the cluster average. Region 13, located apparently “in front” of this subcluster, is marginally hotter than the cluster average, suggesting that there indeed is a mild merger shock and therefore simple projection is unlikely. Our map excludes the possibility of a major merger comparable to the ones seen in A754, A3667 or Cygnus A. The radial temperature profile of this cluster is nearly constant with a probable mild central peak.

A399–A401.—*ASCA* observed this pair with 3 pointings centered at each cluster and between them. Our regions for A401 are sectors of concentric annuli with $r = 0 - 2' - 7' - 14'$ (Fig. 2). In the A399 map, the regions are the same except that the innermost one is centered on the brightness peak while others are centered on the cluster centroid. The overall temperatures for A401, A399, and the link region are in agreement with the earlier *ASCA* analysis of Fujita et al. (1996) that did not take into account the PSF effects. Our analysis ignores the effects of *ASCA* stray light (Ishisaki 1996) that may be important when a bright cluster is just outside the mirror field of view, as in two of these three pointings. However, an estimate shows that such contamination is comparatively small for these observations.

The temperature map shows a centrally symmetric temperature structure in both clusters, with sectors 6 and 16, each point-

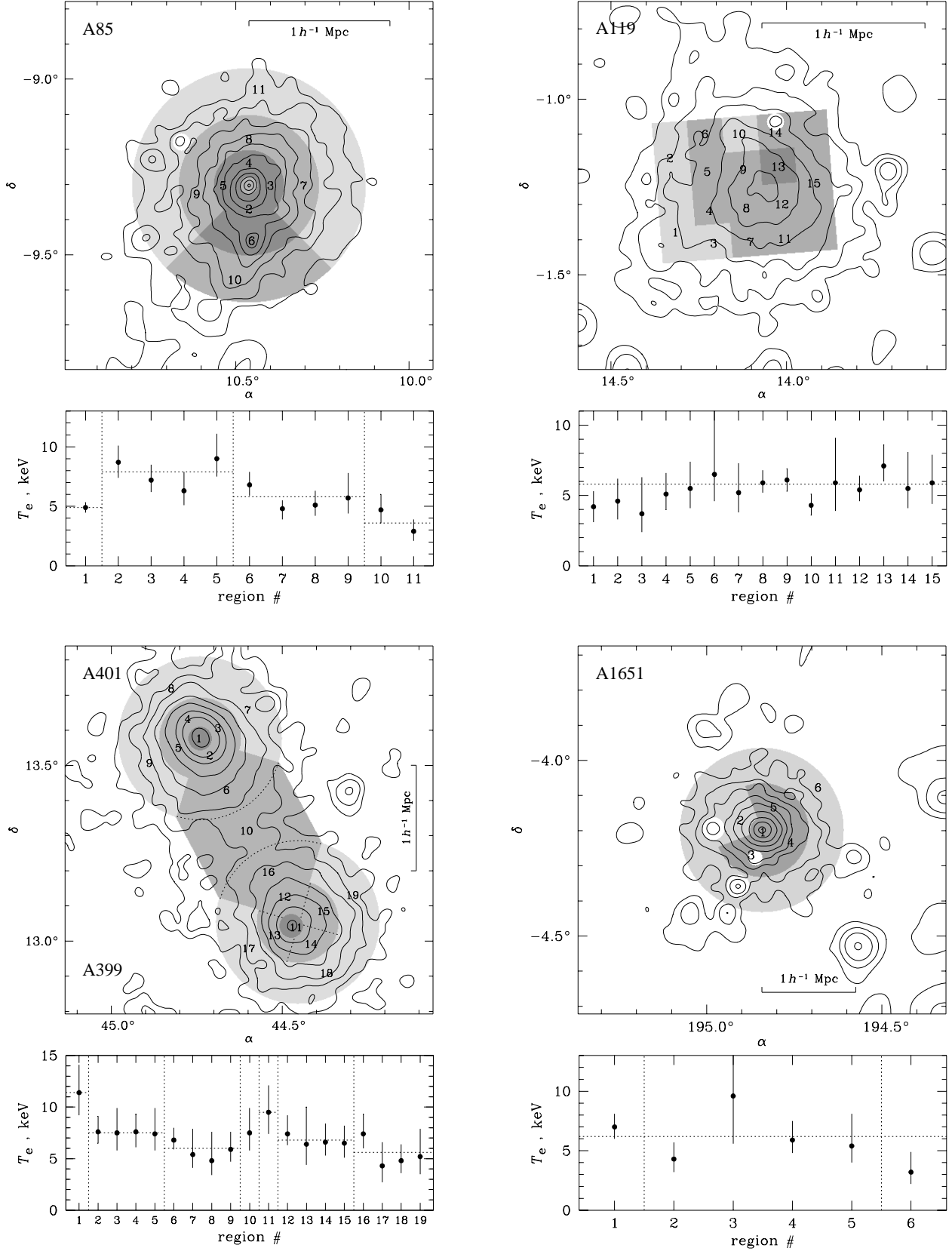


FIG. 2.—Cluster temperature maps. Contours show *ROSAT* PSPC brightness, grayscale shows *ASCA* temperatures. Regions (sectors, boxes, or their combination, delineated by dotted lines in the nonobvious places) are numbered and their temperatures with 90% confidence intervals (including systematics) are shown in the lower panels. Dotted horizontal lines in lower panels show emission-weighted average temperatures either in the annulus or over the whole cluster; dotted vertical lines separate annuli. Point sources excluded or fitted separately are shown as blank circles, but some of them are not shown for clarity.

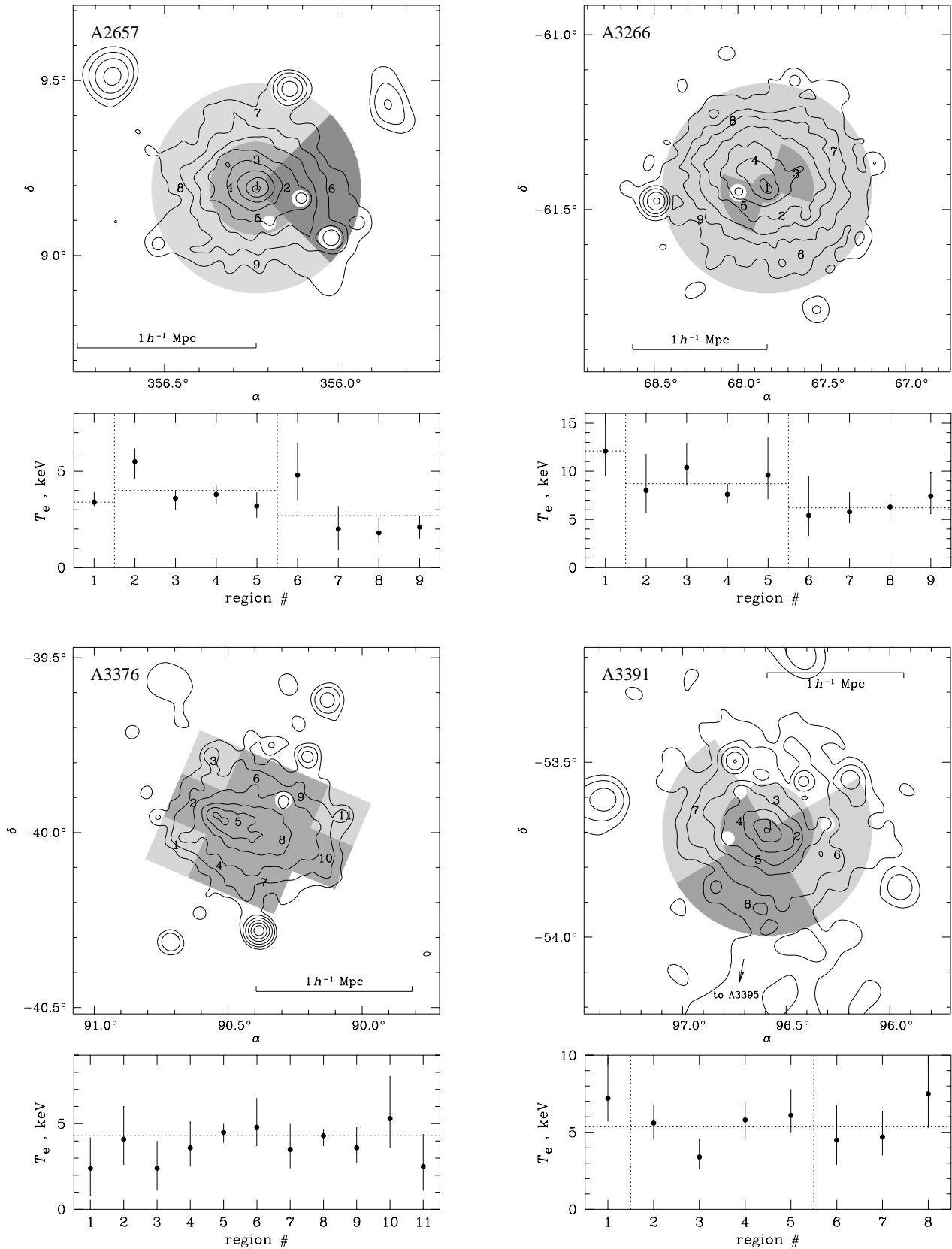


FIG. 2.—Continued

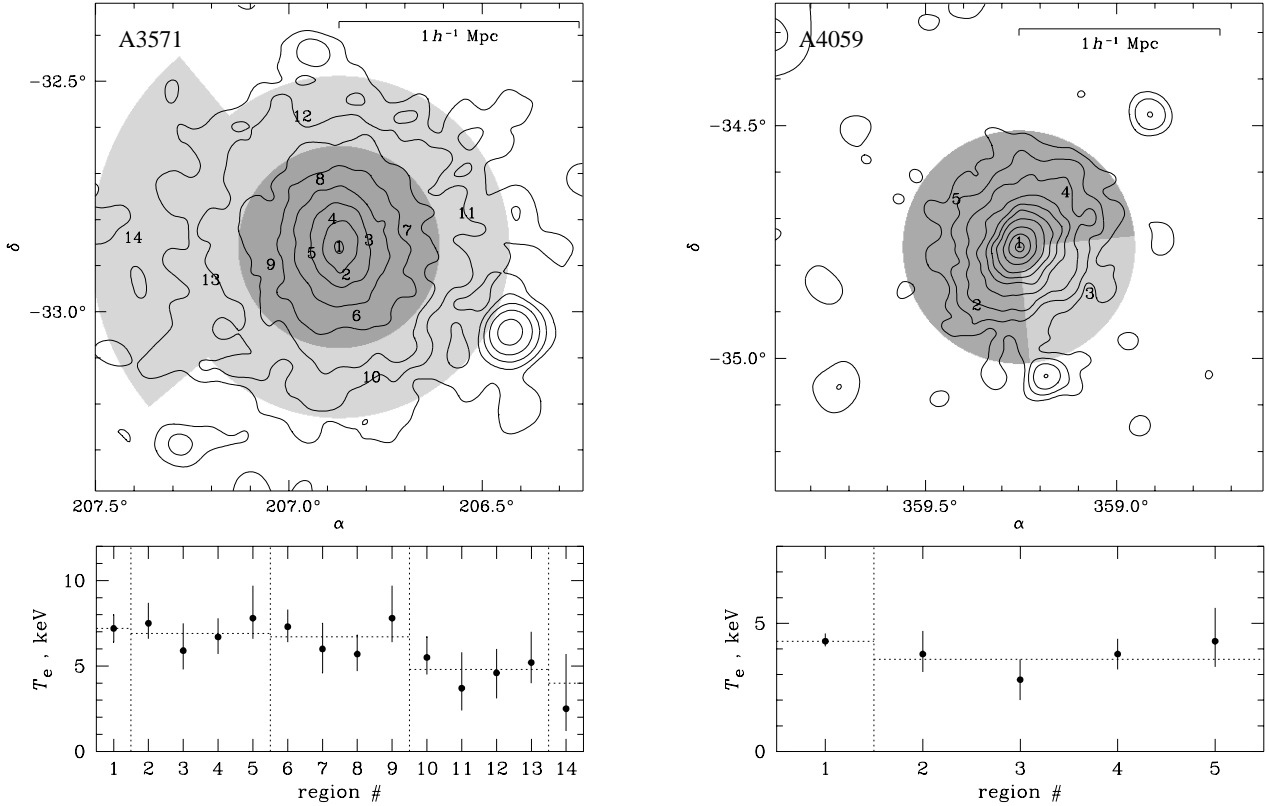


FIG. 2.—Continued

ing toward the opposite cluster, being hotter, with marginal significance, than the corresponding sectors at the same radius. The temperature declines with radius, with peaks in the centers of both of these cD clusters (Fig. 4). Despite the large uncertainty, the gas in region 10 between the clusters does not seem to follow the temperature decline, arguing against projection and possibly suggesting the beginning of a collision of these clusters or a massive dark matter filament between them. Our analysis requires no cooling flow components in these clusters, in agreement with Edge, Stewart, & Fabian (1992). This makes A401 a rather unusual cD cluster since neither the temperature map nor the X-ray image indicate recent merger activity in the central regions of this cluster, and yet it has no cooling flow.

A478.—This distant cluster has a strong cooling flow (e.g., White et al. 1994) and is at the limit of the *ASCA*'s angular resolution. For this reason, reconstruction of its two-dimensional map is currently impossible and even a radial profile (for which we use radii $r = 0 - 1.5' - 6' - 16'$) has very large uncertainties (Fig. 4). We fixed the central temperature, which is also a cooling flow upper temperature, to be equal to that in the surrounding annulus. A central cool component is required at 94% confidence and there is a marginally significant temperature decline with radius.

A644.—This cluster is analyzed in detail by Bauer & Sarazin (1998), who find a merger signature in the temperature map and marginal evidence for a central cooling flow. The temperature declines with radius. Note that our wide-beam temperature in Table 1 differs slightly from their value due to our wider integration region.

A754.—A temperature map of this merging cluster was dis-

cussed in detail in Henriksen & Markevitch (1996). Here we present its radial temperature profile (Fig. 4), although for such a highly asymmetric cluster with complex temperature structure, it does not have much meaning. The profile shows a temperature decline.

A780 (Hydra A).—Ikebe et al. (1997) previously analyzed the same data on this cooling flow cluster with their independent code. We find a temperature decline with radius (Fig. 4) outside the central cluster region similar to that in Ikebe et al., and also detect the presence of cooler gas in the center at greater than 99.9% confidence. A two-dimensional temperature map of this cluster is not given since it would be inaccurate because of the strong cooling flow.

A1650.—This is another example of a distant cooling flow. Our analysis of this cluster with a large cD was complicated by the absence of a PSPC image. Instead, we used the lower-resolution *Einstein* IPC image. As a result, the accuracy of the temperature profile is poor (Fig. 4). A cool central component is detected at 99% confidence.

A1651.—This is a distant cD cluster, for which our data do not require a central cool component. Its PSPC image is rather regular and our temperature map ($r = 0 - 2' - 8' - 14'$ annuli with the second annulus divided into 4 sectors, Fig. 2) shows no interesting structures, although its accuracy is poor. A radial temperature decline is suggested (Fig. 4).

A1736.—For this cluster, included here for completeness, we obtain only a wide-beam temperature (see §3.7). *Einstein* IPC and *ASCA* images indicate that A1736 does not exhibit a strong cooling flow or any bright contaminating sources. Therefore, its weighted temperature T_X should be close to the wide-beam

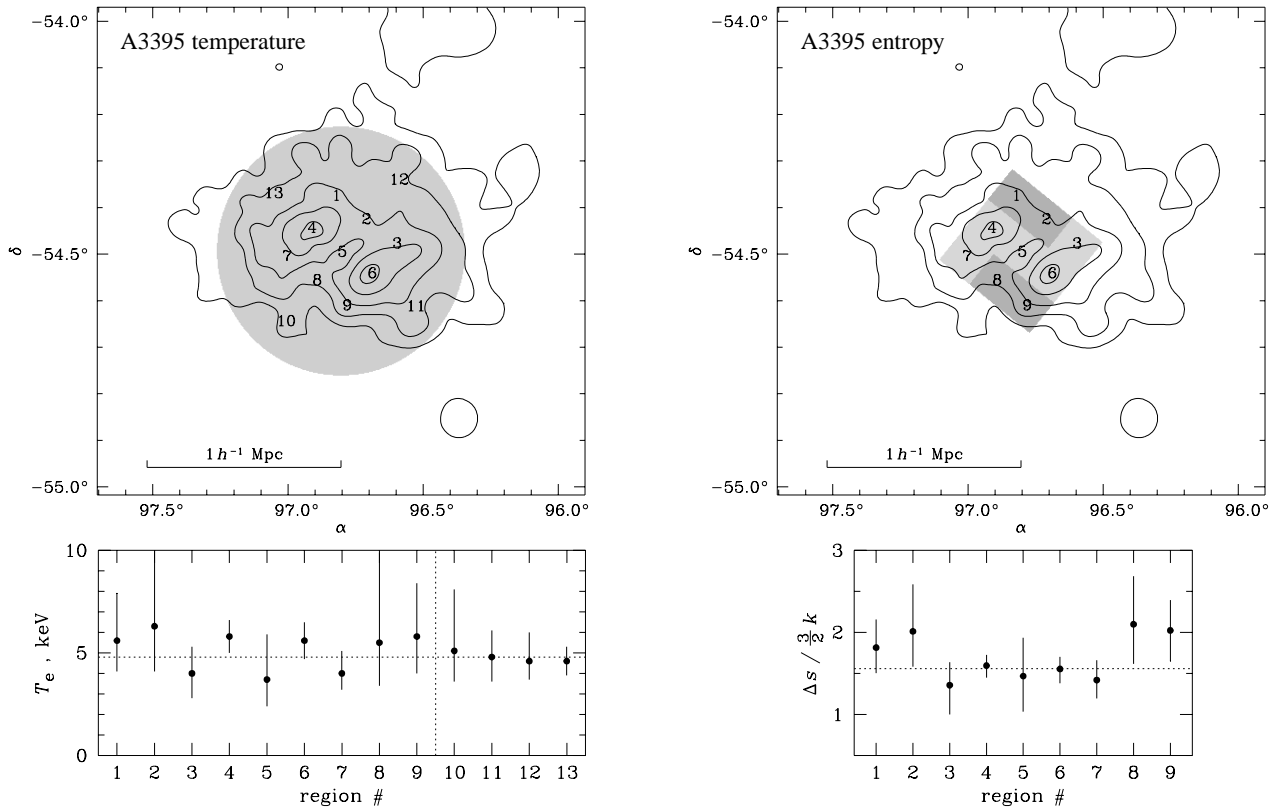


FIG. 3.—Temperature and specific entropy maps of A3395 (see text). Left panels are similar to Fig. 2. Lower right panel shows approximate specific entropy in each region with respect to an arbitrary zero value; horizontal line denotes a weighted mean value. Grayscale in the upper right panel shows these specific entropy values overlaid on the image.

temperature, as for other such clusters (see §5 below); this will be assumed in Markevitch (1998).

A1795.—This cluster has one of the strongest known cooling flows (Edge et al. 1992; Fabian et al. 1994a [an earlier *ASCA* analysis]; Briel & Henry 1996). The cool component is required at greater than 99.9% confidence in the central $r = 1.5'$ region. This small central region contains almost half of the total cluster emission in the *ROSAT* band, which makes our *ASCA* spatially resolved analysis very uncertain. We detect some indication of a radial temperature decline. A bright point source $6'$ from the center was fit separately and found to be equally well described by either a thermal or a soft power law spectrum; this uncertainty does not affect the temperature values in other cluster regions.

Note that our temperatures at all radii are higher than the single-temperature fit to the overall spectrum (Fig. 4 and Table 1); this cluster is the most prominent example of how the presence of a strong cooling flow results in an underestimate of the cluster temperature. This issue will be discussed below.

A2029.—This strong cooling flow and well relaxed cluster is discussed in detail in Sarazin et al. (1997), who detect a significant radial temperature decline in it.

A2065.—A temperature map for this cluster is presented and discussed in M98. A prominent asymmetric temperature pattern is detected, as well as a central cool component (at 99% confidence) which must have survived the ongoing major merger. In Fig. 4, we present its radial temperature profile, which is declining with radius. Dashed cross shows a single-

temperature fit in the central bin.

A2142.—This is the most distant cluster in our sample. Its *ROSAT* PSPC and HRI images suggest an ongoing merger. However, we cannot reconstruct its temperature map due to the presence of a cooling flow (Edge et al. 1992; Henry & Briel 1996) which we detect with greater than 99% confidence. An AGN $4'$ from the cluster center is fitted separately by a power law with the best-fit index of -1.9 . The temperature profile has large uncertainties and is consistent with a constant value, although a temperature decline with radius is suggested (Fig. 4).

A2256.—A detailed discussion of this cluster, including its total mass derivation, is presented in M96 and Markevitch & Vikhlinin (1997b, hereafter MV97b). Those works inferred that, most probably, the two large subclusters of A2256 have not yet started interacting. An ongoing collision between them is excluded, since the temperature map does not exhibit structures characteristic of shock heating, predicted by simulations and indeed observed in several merging clusters such as A754 and Cygnus A. In the discussion below, we use the projected temperature profile for the main component of A2256 obtained in MV97b.

A2319.—GIS results for this cluster were presented in M96. The GIS+SIS results are similar with a small revision of the overall temperature (Table 1). M96 found that there is a cool region near the center coincident with a subcluster seen in the X-ray image. As for A2256, the temperature map does not suggest any major merger, although it has a poorer accuracy than the A2256 map.

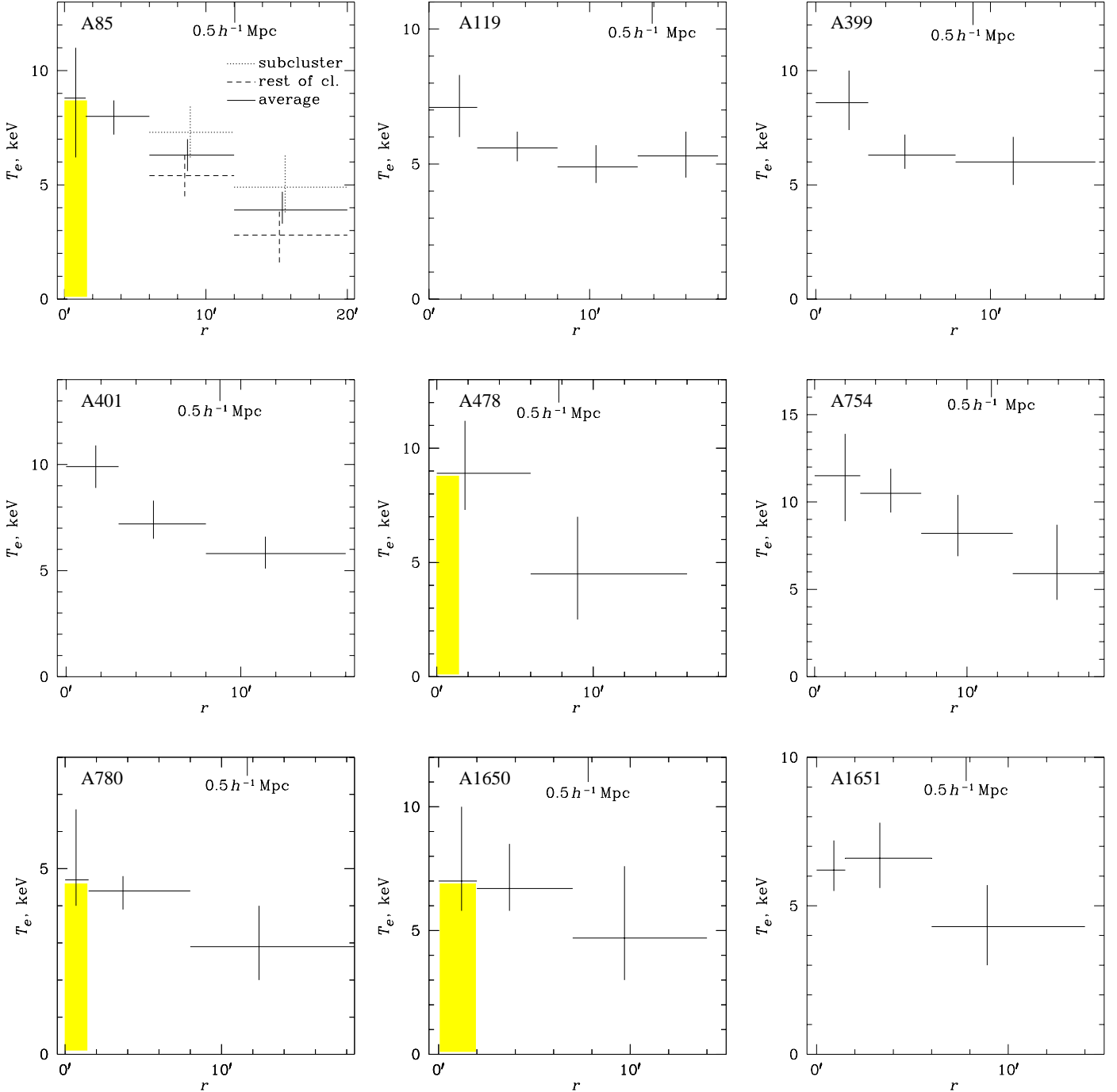


FIG. 4.—Radial projected temperature profiles. Crosses are centered on the emission-weighted radii. Vertical errors are 90% and include systematic uncertainties; horizontal error bars show the boundaries of the annulus. Gray bands denote a continuous range of temperatures in a cooling flow, or a power law component, in those clusters where these spectral components are significantly detected by our analysis. For such clusters, the central cross corresponds to the upper (ambient) temperature of the cooling flow. For illustration, a central single-temperature fit is also shown for A2065 as dotted cross.

A2597.—This is a distant cluster dominated by a cooling flow (e.g., Edge et al. 1992; Sarazin & McNamara 1997). Almost half of the total emission in the *ROSAT* band originates from the central $r = 50 h^{-1}$ Mpc ($0.8'$) region. For this reason, we were only able to fit spectra in two radial bins, $r = 0 - 1.5' - 15'$, to separate the cooling flow from the rest of the cluster. The cooling flow sufficiently dominated the central bin

that we could not determine an independent temperature there, so we assumed that the ambient temperature was constant at all radii. A cool component is required at greater than 99% confidence in the central region.

A2657.—A slight westward elongation apparent in the image coincides with significantly hotter sectors in the temperature map (consisting of sectors of $r = 0 - 1.5' - 7' - 18'$ annuli,

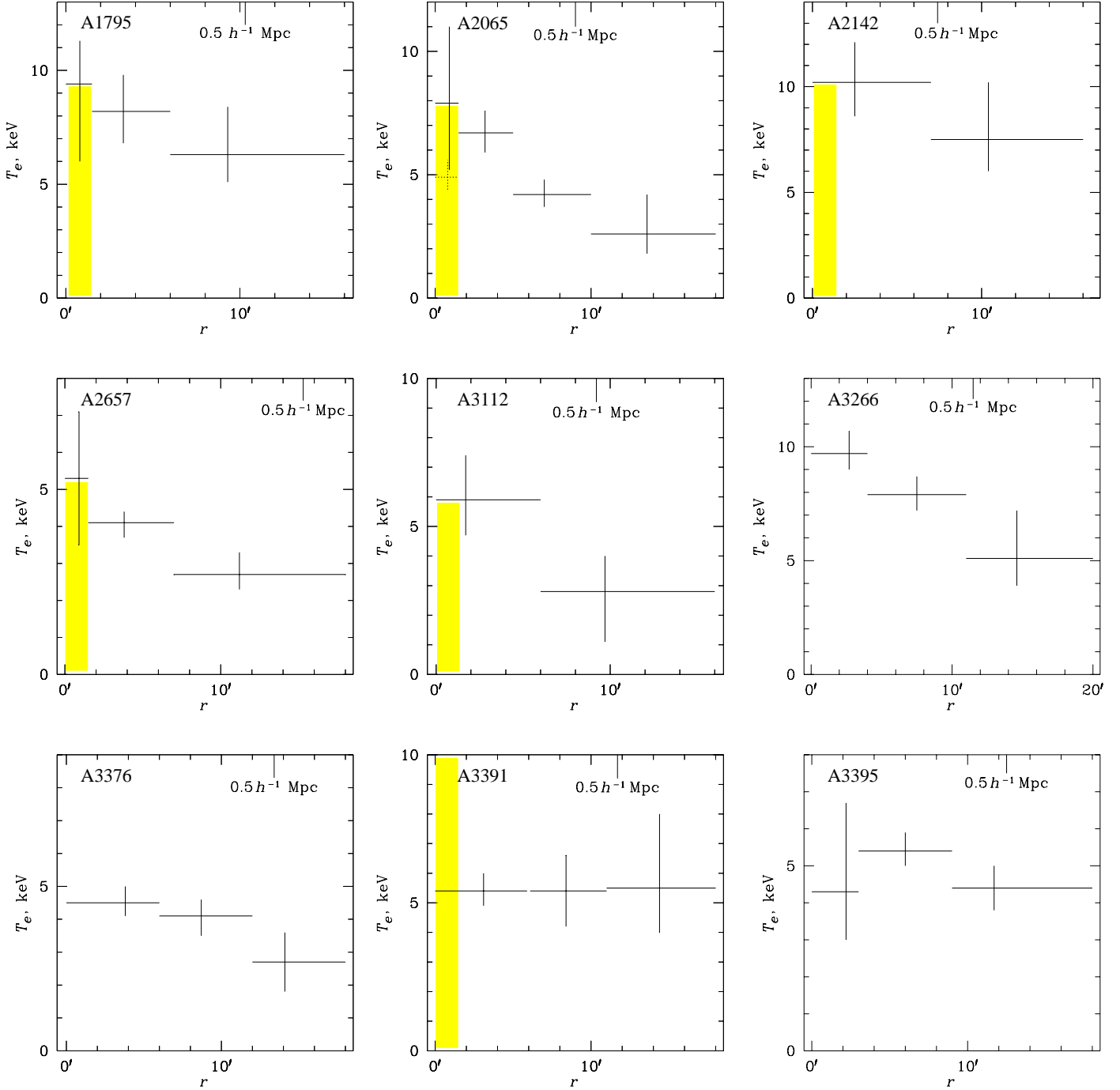


FIG. 4.—Continued

Fig. 2), indicating a merger rather similar to that in A85. We detect a moderate central cooling flow with 94% confidence (the map shows a single-temperature fit). The azimuthally averaged temperature declines with radius (Fig. 4). A point source south of center (white circle in region 5) is an AGN for which we obtain $\gamma = -1.60 \pm 0.16$.

A3112.—This cluster possesses a strong cooling flow (Edge et al. 1992) which we detect at 98% significance. Again, for this reason, the radial temperature profile has a large uncertainty. Still, there is a significant indication of a radial temperature decline (Fig. 4).

A3266.—A *ROSAT* PSPC image of this cluster indicates ongoing merger. Our temperature map (which consists of sectors of annuli with $r = 0 - 2.5' - 8' - 18'$ centered on the brightness peak, Fig. 2) does not have sufficient resolution, but may indeed suggest an asymmetric temperature pattern expected for a merger. Sector 4, which is coincident with an infalling sub-cluster, is cooler than the annulus average, while the neighboring sector 3 is hotter, although with only marginal significance. The cluster brightness peak is hot; on average, the temperature declines with radius (Fig. 4).

A3376.—A temperature map of this cluster (made of $8' \times 8'$

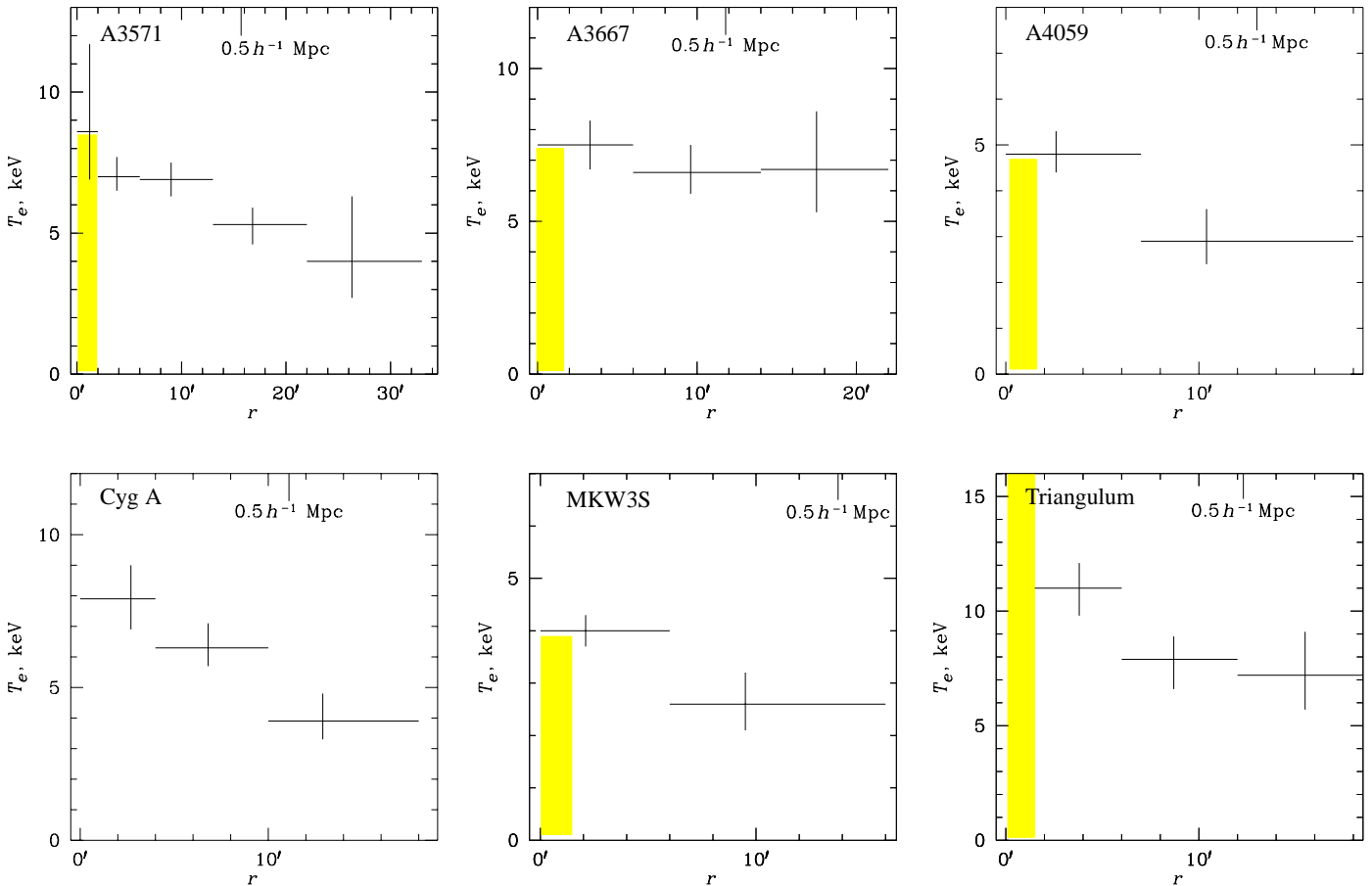


FIG. 4.—Continued

boxes) is shown in Fig. 2. A comet-like shape of the *ROSAT* image indicates a merger. However, our temperature map probably excludes any strong shocks. A radial profile (Fig. 4) shows that the outer cluster regions are significantly cooler than the center, although a radial profile has little meaning for this asymmetric cluster. This object is at the lower flux limit of our sample and only has a short GIS exposure, so our results are limited by statistics.

A3391.—This relatively regular-looking cluster and A3395 form a pair separated by $48'$ or $2h^{-1}$ Mpc in projection, similar to the A399-A401 pair. Stray light contamination from the neighboring cluster is estimated to be small. Our temperature map consists of sectors of annuli with $r = 0 - 2' - 8' - 18'$ (Fig. 2); the cluster northern region does not have sufficient *ASCA* coverage and is not shown (but was included in the fit). As in the A399-A401 pair, the sector pointing toward A3395 is marginally hotter, suggesting that the two clusters are beginning to collide or are connected by a massive filament. There is some temperature asymmetry in the cluster’s inner $0.7h^{-1}$ Mpc as well, possibly a remnant of earlier mergers. The azimuthally averaged temperature is constant with radius (Fig. 4). In the central radial bin, we detect an additional spectral component best described by an absorbed power law. If its slope is fixed at -1.7 , the redshifted absorbing column is between $0.3 - 80 \times 10^{21} \text{ cm}^{-2}$. The normalization of this component is greater than zero at 92% confidence. In Fig. 2, a single-temperature fit is shown for the central region, while in Fig. 4,

the result of including the additional spectral component (denoted by gray band) is shown.

A3395.—A temperature map of this double cluster is shown separately from others in Fig. 3. Regions of the map are nine $5' \times 5'$ boxes, with boxes 4 and 6 coincident with the peaks of the two subclusters, and four sectors of an $r = 16'$ circle outside the boxes. The temperature map excludes the presence of a very hot gas between the cluster peaks (region 5) which one would expect if the two clusters were colliding head-on. The peaks (regions 4 and 6) are marginally hotter than the cluster average, but temperatures in other regions are consistent with the average within their large uncertainties. The uncertainties are large mostly because of the low statistics of the *ROSAT* PSPC image obtained from a very short (2 ks) exposure.

A closer look at the elongated X-ray images of each of the two A3395 components suggests that they may in fact be in the course of an offset merger, with the northeast and southwest peaks moving west and east, respectively. Interestingly, the statistically insignificant positive temperature deviations are observed in regions 1, 2, 8, and 9 “in front” of the subclusters if this speculation is correct. Entropy maps are a sensitive indicator of shock heating (MSI) and may reveal additional detail. We show in Fig. 3 (right panel) approximate specific entropies of the gas in the inner 9 cluster regions. The entropy per particle is defined here as $\Delta s \equiv s - s_0 = \frac{3}{2}k \ln [(T/T_0)(\rho/\rho_0)^{-2/3}]$, where the subscript 0 refers to any fiducial region in the cluster. For a qualitative estimate, we approximate $\rho/\rho_0 \sim (S_x/S_{x0})^{1/2}$,

where S_x is the cluster X-ray surface brightness in a given region. This approximation is adequate in the central regions but is inaccurate in the outer image regions which are not shown (the entropy values there are higher than in the center as in any isothermal cluster). With marginal significance, regions 1, 2, 8, and 9 have higher specific entropy than other central regions which appear to be approximately adiabatic. Note that region 5, between the peaks, has a low density similar to those in high-entropy regions, but has an average entropy. Such an entropy distribution suggests the presence of shock-heated gas in front of each of the two subclusters, which should then indeed collide as proposed above. We note that, of course, dividing temperatures by a power of surface brightness to calculate entropy does not increase the statistical significance of the observed temperature structure, but it helps to present it in a more illuminating way. From the observed entropy differences one can estimate, for example, the relative velocity of the colliding subclusters; however, any quantitative analysis must wait for more accurate measurements.

A3558.—This cluster is analyzed in MV97a, who detected temperature structure indicating a major merger, and a slow radial temperature decline. The region around the central galaxy requires a cool and a hot or nonthermal component.

A3571.—This cluster has the best-quality data in our sample. Temperatures are obtained in 90° sectors for annuli with $r = 0 - 2' - 6' - 13' - 22' - 35'$. In the last annulus, only two sectors are covered by *ASCA*; in one of them, the individual temperature is not usefully constrained and is not shown in Fig. 2, but it is included in the calculation of the radial profile. The map in Fig. 2 shows no significant deviations from azimuthal symmetry, except for the possibility that the southern half of the cluster may be slightly hotter than the northern half. Together with the symmetry of the cluster image, the featureless temperature map suggests that A3571 is a well-relaxed cluster. This cluster is known to have a small cooling flow (Edge et al. 1992); a central cool component is detected with 92% confidence in our data. The radial temperature profile, shown in Fig. 4, will be used for a derivation of the total mass profile in a separate paper.

A3667.—A temperature map of this cluster shows an ongoing major merger and is presented and discussed in detail in M98. A trace of cooler gas, which must have survived a merger, is detected in the vicinity of the central galaxy with 95% confidence. The radially-averaged temperature profile (Fig. 4) is constant; however, a radial profile has little meaning for this highly asymmetric cluster.

A4059.—This is a cooling flow cluster (e.g., Huang & Sarazin 1998); we detect a central cool component with 99% confidence. A crude temperature map (which consists of two annuli with $r = 0 - 3' - 16'$ with the outer one divided into 4 sectors, Fig. 2) shows no significant detail. A single-temperature fit for the central region is shown in the map. A radial profile shows a significant temperature decline with radius (Fig. 4).

Cygnus A.—A temperature map of this cluster is presented in M98. The map reveals temperature structure indicating an ongoing merger of two large subclusters seen in the X-ray image (and perhaps in the optical as well; Owens et al. 1997), one of which harbors a strong radio galaxy Cygnus A. There is a strong point source at the position of Cygnus A in the hardest-band *ASCA* images where the surrounding cluster emission is faint, which shows that *ASCA* can confidently separate the AGN

component from the cluster. Fitting the cluster temperatures simultaneously with a self-absorbed power law in a $r = 1.5'$ region centered on the AGN, we obtain for the AGN component a slope of $-2.0_{-0.4}^{+0.3}$ and a column density of $4.8_{-1.1}^{+1.2} \times 10^{23} \text{ cm}^{-2}$, in agreement with the *Ginga* wide-angle fit (Ueno et al. 1994). The temperature of the surrounding cluster component is also in agreement with Ueno et al. Reynolds & Fabian (1996) detect a cooling flow around Cygnus A in the *ROSAT* data. A cooling flow component is not required in our fit, nor is it excluded, due to the spectral complexity of the AGN region. A radial profile, centered on the cluster large-scale centroid between the colliding subclusters, is shown in Fig. 4.

MKW3S.—This apparently relaxed, slightly elliptical cluster has a strong cooling flow which we detect with 96% confidence. Because of this, the temperature map does not have useful accuracy and is not presented. The temperature declines with radius (Fig. 4).

Triangulum Australis.—Temperature, pressure, and entropy maps of this hot cluster are discussed in MSI, who find an indication for nonadiabatic heating of the intracluster gas. Here we present the cluster's radial temperature profile. MSI noted a problem with the fit to the central $r = 3'$ region of this cluster. A smaller, $r = 1.5'$ central bin which we use here (in addition to including lower-energy *ASCA* data) requires an additional spectral component with 99% confidence. From *ASCA* data alone, we cannot distinguish between a power-law and a cooling flow component with a high upper temperature. *ROSAT* PSPC data which are sensitive to the presence of cool gas, do not require a cooling flow (MSI), therefore, a nonthermal contribution is more plausible. A complex spectrum in the central radial bin, denoted by the gray band in Fig. 4, does not significantly affect measurements in the outer annuli. The profile shows the temperature rising toward the cluster center.

5. CORRECTING AVERAGE TEMPERATURES FOR COOLING FLOWS

We noted above that the presence of a strong cooling flow results in a significant underestimate of the average temperature for some clusters. The possibility of such underestimates was suggested earlier by Fabian et al. (1994b) as one explanation for the observed difference in the $L_x - T$ relations for clusters with and without cooling flows. However, because spatially resolved spectral data for clusters were unavailable, those authors did not foresee the amplitude of the underestimate that we observe (for even more extreme examples see, e.g., Allen 1998). Since cooling flows occupy a small fraction of the cluster volume and are governed by different physics than the rest of cluster gas (for a review see, e.g., Fabian 1994), their contribution should be excluded from the temperature estimates, if one intends to compare the global cluster properties with theoretical and numerical predictions that at present cannot model radiative cooling in detail.

The temperature maps and profiles presented above provide the necessary data to calculate average, emission-weighted gas temperatures corrected for cooling flows and any unrelated sources that contaminated earlier, unresolved data. To do this, we co-add the fitted temperatures, T_i , for all regions of a cluster map or a profile with weights proportional to the *ROSAT* flux, f_i , from the respective i -th region (which for the temperature range of our sample essentially means weighting with the emission measure). For regions with cooling flows or other contaminating components (assigned $i = 1$ below), only the main thermal (ambient) component, T_1 , was included in the calculation

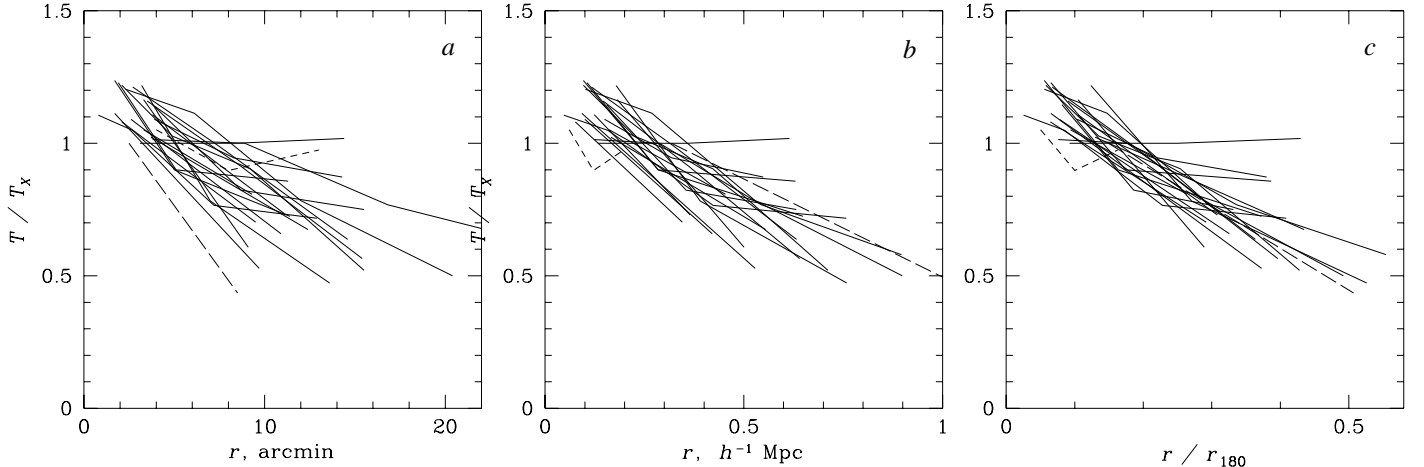


FIG. 5.—Normalized temperature profiles of 19 relatively symmetric clusters, plotted against radii in (a) arcminutes, (b) megaparsecs, and (c) in units of r_{180} . Cooling flow components are removed. Error bars and central temperatures with large uncertainties are not shown for clarity. Also shown for comparison are nearby AWM7 (short-dashed line) and distant A2163 (long-dashed line), which are not part of the sample. Cluster profiles are quite different in detector units (a), but appear rather similar in physical units (b and especially c). The biggest deviation in panel (c) is A3391, which is still consistent with others within its errors (see Fig. 7 and discussion in §7.2.4).

of the weighted temperature T_X :

$$T_X = \frac{T_1 f_1 \eta_1 (1 - \eta_{cf}) + \sum_{i=2}^n T_i f_i}{f_1 \eta_1 (1 - \eta_{cf}) + \sum_{i=2}^n f_i}. \quad (1)$$

Here, η_1 denotes the overall normalization of region 1 relative to that given by its *ROSAT* flux and η_{cf} denotes the fraction of the excluded spectral component in the projected emission measure of region 1, both fitted as free parameters (see §3.3). Confidence intervals on T_X were calculated by Monte-Carlo simulations to take into account correlations between the temperature measurements in different regions. Using a map or a profile for this procedure did not result in significant differences in the weighted temperatures. Although in reality the temperature changes continuously rather than abruptly as in our maps, each T_i in turn is, essentially, the emission-weighted temperature over the respective region, thus the approximation (1) is sufficient for our level of accuracy. Despite its simplicity, our treatment of central regions is adequate even for strong cooling flows, because for those clusters η_{cf} is near 1 and the contribution of the central region to T_X is small anyway.

The resulting weighted temperatures are given in Table 1. The table shows that, as expected, the weighted temperatures are consistent with the single-temperature fits for clusters without cooling flows or other obvious spectral complications. Strong cooling flow clusters have significantly higher mean temperatures than their single-temperature fits imply, with the greatest difference, by a factor of 1.3, obtained for A1795. A separate paper (Markevitch 1998) shows that the difference between the $L_X - T$ relations for clusters with and without cooling flows essentially disappears when these weighted temperatures and the luminosities with excised cooling flows are used. Such an improvement strongly suggests that our measurements indeed result in more physically meaningful temperatures. We will use these temperatures below to normalize the radial temperature profiles and estimate cluster virial radii.

Figure 4 shows that, with a few exceptions, cluster temperatures significantly decline with radius. Those few clusters that do not show a general temperature decline are mostly ongoing mergers (e.g., A3667) or highly asymmetric clusters (e.g., A3395) for which radial profiles do not have much physical meaning. Below we show that temperature profiles of almost all azimuthally symmetric clusters are similar when compared in physical units.

We normalize the radial temperature profile for each cluster by the weighted average temperature T_X obtained in §5, and plot it against the radius in units of r_{180} , within which the mean density (total mass divided by volume) is 180 times the critical density. This radius is approximately the radius of the virialized region for clusters (the virial radius) in an $\Omega = 1$ universe (e.g., Lacey & Cole 1993). It is natural to scale radii by the virial radius, because cluster total density profiles are expected to be similar in these units (e.g., Bertschinger 1985). The scaled radii are independent of the Hubble constant.

The values of r_{180} can in principle be derived directly by reconstructing the mass distribution using the gas temperature and density profiles, if the cluster gas is in hydrostatic equilibrium. However, only several clusters in our sample have sufficiently accurate data and symmetric images for such a determination (MV97b; Sarazin et al. 1997; our ongoing work). Alternatively, simulations of Evrard, Metzler, & Navarro (1996, hereafter EMN) predict that the average cluster temperature strongly correlates with the cluster mass, even for moderately irregular clusters. We take advantage of this correlation to calculate r_{180} for all clusters in a uniform manner, using our weighted temperatures and the EMN fit to the simulations, $r_{180} = 1.95 h^{-1} \text{Mpc} (T_X / 10 \text{ keV})^{1/2}$. Although the simulations generally do not reproduce the observed temperature profiles (see §7.2.3 below) and, therefore, this relation may be inaccurate, we are mostly interested in the scaling of r_{180} with T_X which is unlikely to be seriously wrong. We exclude from this exercise all 5 clusters with $z > 0.08$ (A478, A1650, A1651, A2142, and A2597) because of large errors in their profiles, and 6 clusters with strongly asymmetric images (A119, A754, A3376, A3395, A3667, and Cygnus A) because their radial pro-

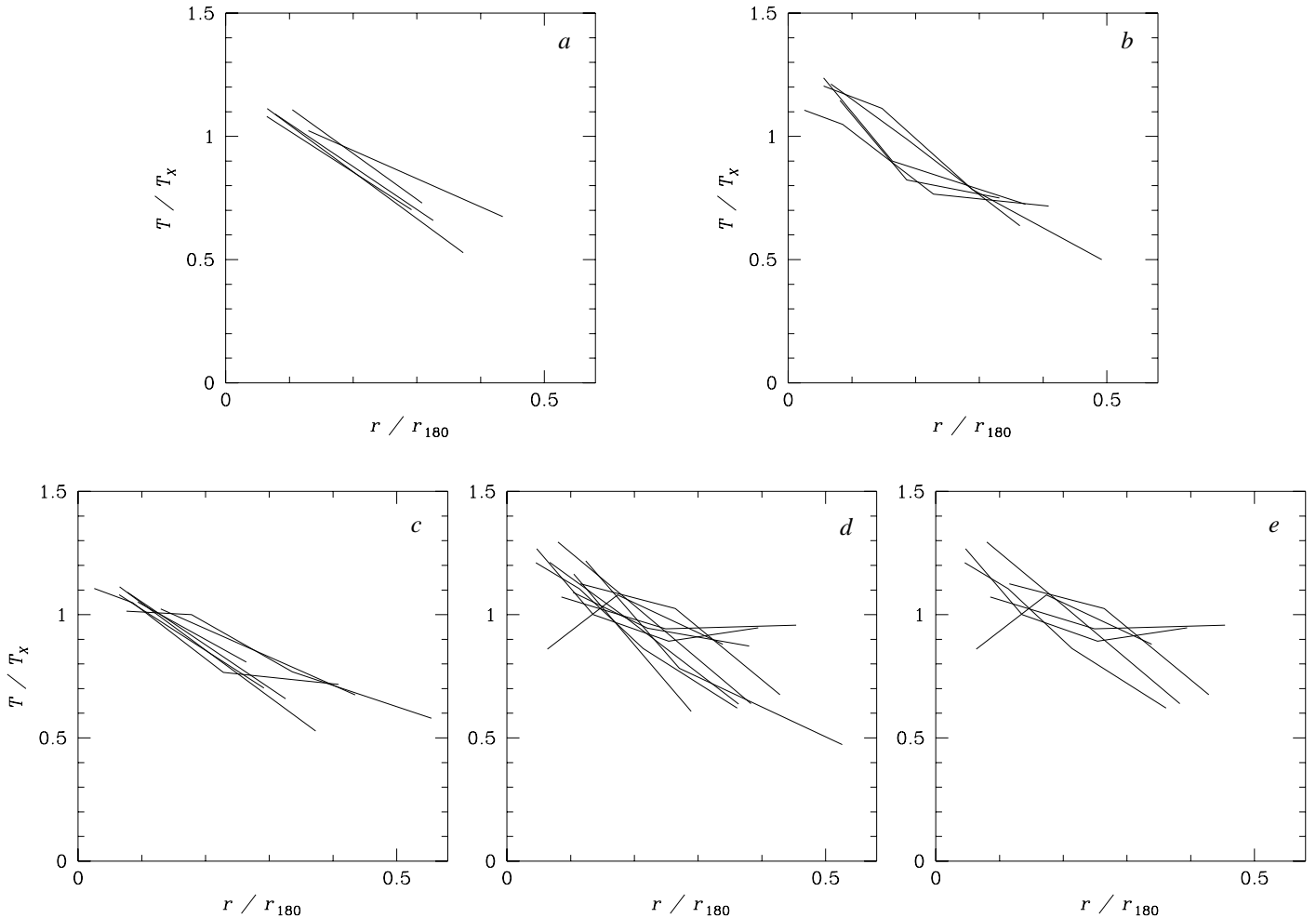


FIG. 6.—Normalized temperature profiles of several cluster subsets. Error bars are omitted for clarity. Panels (a) and (b) show five coolest ($T_x \leq 5.3$ keV) and five hottest ($T_x \geq 8$ keV) clusters of those shown in Fig. 5 (excluding AWM7 and A2163), respectively. Panel (c) shows relaxed clusters with cooling flows (A780, A1795, A2029, A3112, A3571, A4059, MKW3S), panel (d) shows asymmetric and strong merger clusters (A119, A644, A754, A2065, A3266, A3376, A3395, A3558, A3667, Cygnus A), and panel (e) shows only the asymmetric clusters excluded from Fig. 5 (A119, A754, A3376, A3395, A3667, Cygnus A). There is no apparent systematic difference between the subsamples, except for a greater scatter and slightly less steep decline of profiles for irregular clusters (panels *d* and *e*).

files have little meaning. Note that we do not specifically exclude mergers but only those of them with asymmetric images, due to the above consideration. For comparison, we include projected temperature profiles for two clusters that are not part of the sample due to their redshifts, A2163 at $z = 0.201$ from M96, and AWM7 at $z = 0.018$ from MV97a.

Figure 5 shows normalized temperature profiles (without error bars for clarity) plotted together against radius in arcminutes, megaparsecs, and in units of r_{180} . Those central temperature values with large uncertainties (resulting from the removal of the cooling flow component) are not shown. It is clear from the figure that in angular (detector) units, clusters have quite different temperature profiles. However, the profiles become rather similar in linear distance units and still more similar, with just one exception, when plotted against radius in units of r_{180} . This comparison strongly suggests that we are observing a physical temperature decline rather than some unaccounted for instrumental effect.

In Fig. 6(a, b), we plot two subsets of the clusters shown in Fig. 5, the five coolest ($T_x \leq 5.3$ keV) and hottest ($T_x \geq 8$

keV) clusters. There is no apparent systematic difference between them. Note that if we were accounting for the ASCA PSF incorrectly, one would expect systematic differences between cooler and hotter clusters, because the effects of PSF scattering are greater at higher energies. Panels *c*, *d*, *e* in Fig. 6 show, respectively, temperature profiles for strong cooling flow clusters that are thought to be the most relaxed, strong mergers and asymmetric clusters (including those not shown in Fig. 5), and only the asymmetric clusters excluded from Fig. 5. There is no strong qualitative difference between the profiles in these subsets except for the large scatter for asymmetric clusters, and a possibly shallower median slope for the excluded clusters. The shallower slope is in part due to the fact that our profiles are not centered on the brightness peaks but centered on the large-scale emission centroids between the subclusters. Normalized profiles of the five high-redshift clusters in our sample that we do not use because of large errors are consistent with the others.

We now try to quantify the slope of our composite radial temperature profile using a polytropic relation. Figure 7 shows profiles of symmetric clusters (those in Fig. 5 excluding AWM7

and A2163). Also plotted is an approximate band that encloses most profiles and their error bars. We assume a gas distribution with the core radius $a_x = 0.15 h^{-1}$ Mpc and $\beta = 0.67$ typical for our cluster sample median temperature of 7 keV (Jones & Forman 1997), and $r_{180} = 1.63 h^{-1}$ Mpc which corresponds to this temperature. The observed temperature decline between 1 and $6 a_x$ (0.09 and $0.55 r_{180}$) in Fig. 7 corresponds to a polytropic index $\gamma \simeq 1.24^{+0.20}_{-0.12}$. The error on γ corresponds to the width of the 90% error band at large radii as shown in Fig. 7. A simple polytropic dependence is not a particularly good description of the composite profile; the ratio of temperatures between 1 and $3 a_x$ corresponds to $\gamma \simeq 1.19$ while the ratio between 3 and $6 a_x$ corresponds to $\gamma \simeq 1.29$. For individual clusters, this equivalent polytropic index would of course depend on the individual gas density profile and the appropriate scaling of r_{180} , and in fact may be quite different from these values. We did not attempt to derive a more physically motivated functional form for the composite temperature profile. It should be searched for among the solutions of the hydrostatic equilibrium equation for various forms of the dark matter distribution; this issue will be addressed in a separate paper.

7. DISCUSSION

7.1. Merger and Cooling Flow Fractions

The last column in Table 1 marks those clusters in which our temperature maps (or entropy maps for A3395 and Triangulum Australis) indicate significant merging. In addition, *ROSAT* images of A2142, A3266, and A3376 undoubtedly indicate mergers in progress; for these clusters, we were unable to obtain sufficiently accurate spatially resolved temperatures due to limited angular resolution or statistics. Thus, in total, about half of the sample shows signs of ongoing mergers. The frequency of mergers is an indicator of the cluster formation rate which depends on cosmology (e.g., Richstone, Loeb, & Turner 1992). Temperature maps of mergers provide information complementary to that contained in the X-ray image, such as evidence for physical interaction, the merger direction, the collision velocity, etc. This makes temperature maps potentially more discriminating between cosmological models than tests based on the frequency of substructure in images alone (e.g., Tsai & Buote 1996; Thomas et al. 1997). Therefore, a detailed comparison of the merger fraction in our sample with simulations capable of modeling shocks may yield interesting cosmological constraints.

Table 1 also shows that we detect cooling flow spectral components in about 60% of the sample. We may have missed a few cooling flows (e.g., Cygnus A) due to the *ASCA* limited angular resolution. The fraction of clusters with cooling flows is in general agreement with predictions of Edge et al. (1992) from their *EXOSAT* image analysis.

7.2. The Composite Temperature Profile

The main result of our paper is the observed similarity of most cluster temperature profiles in units of average temperatures and virial radii. We discuss some implications of this finding below, after commenting on relevant earlier work.

7.2.1. Comparison with Earlier Work

Since *ASCA* is the first instrument offering the possibility of (almost) direct spatially resolved cluster temperature measurements, it is difficult to find accurate earlier data with which to

compare our findings. Pre-*ASCA* spatially resolved temperature measurements were mostly limited to the nearby clusters Coma and Perseus. The Coma radial temperature profile obtained by Hughes et al. (1988) from *EXOSAT* is in rather good qualitative agreement with our composite profile. The *Spacelab-2* profile for Perseus (Eyles et al. 1991) only covers relatively small radii, but it agrees with our composite profile when the cooling flow is taken into account. Modeling data from *Einstein* SSS and *HEAO-1* that have different fields of view, Henriksen & White (1996) find that several cooling flow clusters, including A85 and A1795, have components outside the cooling flow regions that are hotter and cooler than the single-temperature fit. This is qualitatively similar to what we find in our direct measurements. MV97a obtained a temperature profile for A2256 using *ROSAT* PSPC which is in excellent agreement with the *ASCA* profile, although with large errors due to the limited PSPC energy band.

Other spatially-resolved *ASCA* temperature measurements are available; we discuss only those which properly include the effects of the PSF. The Ikebe et al. (1997) results for the Hydra A cluster are similar to our independent analysis. The *ASCA* analyses of the outer regions for nearby relatively regular clusters such as Perseus, Coma, and AWM7 are complicated by the presence of stray light; nevertheless, some preliminary results have appeared. Honda et al. (1996) have derived a temperature map for Coma which may indicate some radial temperature decline, although Coma appears to have a complex temperature structure. (T. Ohashi 1997 communicates that a more sophisticated reanalysis results in even greater temperature variations.) A nearly isothermal temperature profile obtained by Ezawa et al. (1997) for the symmetric cluster AWM7 apparently disagrees with our composite profile; however, when a central cooling flow is taken into account (MV97a), the temperature in the central region increases as in other cooling flow clusters. The resulting AWM7 profile is consistent with the observed range of profiles. A definitive check of our results should be possible in the near future with *AXAF*.

7.2.2. Effect on Mass Estimates

The temperature profile is critical in deriving the gravitating mass under the assumption of hydrostatic equilibrium (e.g., Sarazin 1988). To evaluate the effect of the observed temperature decline on the mass estimates, we take a polytropic temperature profile with $\gamma = 1.24$ which approximately represents our data for a typical 7 keV cluster (see §6). For the gas density parameters used in §6, the mass estimates within 1 and 6 core radii (0.15 and $0.9 h^{-1}$ Mpc) are approximately factors of 1.35 and 0.7 of the isothermal β -model estimates, respectively. This is similar to the results of a more detailed modeling of the A2256 *ASCA* data presented in MV97b (who find that the dark matter profile of the Navarro, Frenk, & White 1997 form was marginally allowed by the data but a steeper profile was preferred). It is also qualitatively similar to the A2029 *ASCA* analysis in Sarazin et al. (1997). As discussed in MV97b, the increased mass at small radii and decreased mass at large radii have several important implications. One of them is the convergence of the X-ray and lensing mass estimates at the cluster central regions; Miralda-Escudé & Babul (1995) first noted that a temperature decline such as those we observe would be sufficient to explain most of the mass discrepancy in A2218. Another implication is a steep rise of cluster baryon fraction with

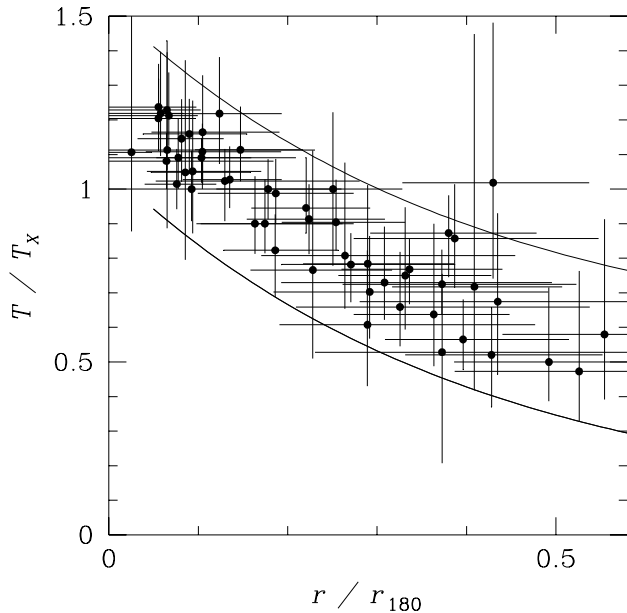


FIG. 7.—Normalized profiles of symmetric clusters (those shown in Fig. 5 without AWM7 and A2163) with their 90% errors. Again, cooling flow components are excluded. Smooth curves show an approximate band that encloses profiles and most of their errors. The outlier is A3391.

radius, which leads to a more pronounced “baryon catastrophe” (e.g., White et al. 1993) and probably indicates a presence of sources of gas thermal energy other than gravity and merger shocks (e.g., David et al. 1995). A model-independent estimate of the average cluster total mass distribution using our composite temperature profile will be attempted in a later paper.

7.2.3. Comparison with Cluster Simulations

In Fig. 8, our composite temperature profile is shown by the light gray band which corresponds to the error band in Fig. 7, and by a less conservative dark gray band which approximates the scatter of the best-fit profile points. Overlaid on the data are radial temperature profiles from several published hydrodynamic cluster simulations with spatial resolution comparable to that of our measurements. We plot median temperature profiles for the simulated cluster samples from EMN (see also references therein), and the average profile from Eke, Navarro, & Frenk (1997; hereafter ENF). We also show profiles of single clusters whose growth was simulated by Katz & White (1993, hereafter KW; further details given in Tsai, Katz, & Bertschinger 1994) and Bryan & Norman (1997, hereafter BN). The smallest radii that we show represent the claimed spatial resolution in the simulations.

For the two steep KW and BN three-dimensional (i.e., not projected) temperature profiles, we performed the emission-weighted projection using the gas density distributions presented in the respective papers. Profiles from EMN and ENF

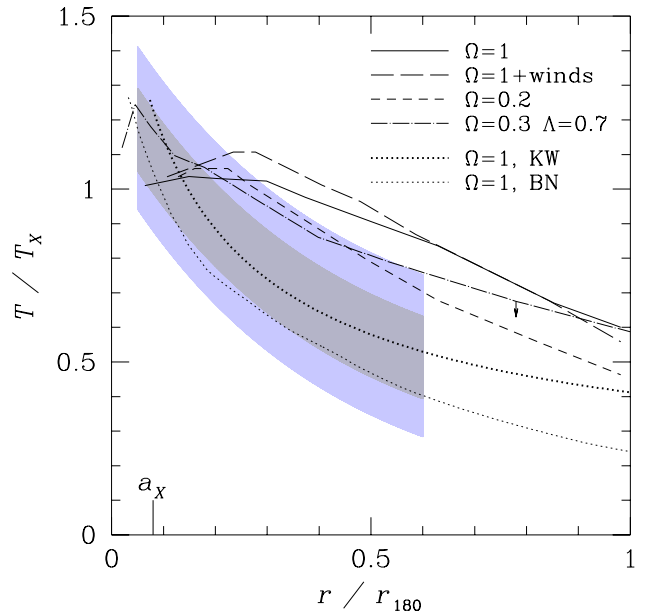


FIG. 8.—Temperature profiles from cluster simulations overlaid on our results. Light gray band is the same as that in Fig. 7; dark gray band encloses only the scatter of the best-fit values in Fig. 7. An approximate X-ray core radius for a 7 keV cluster is marked. Three-dimensional average profiles for $\Omega = 1$, $\Omega = 1 + \text{winds}$, and $\Omega = 0.2$ models are from Evrard et al. (1996); $\Omega = 0.3$, $\Lambda = 0.7$ model is from Eke et al. (1997). Projection effect is shown by an arrow. Also shown are projected profiles from simulations of single clusters of Katz & White (1993) and Bryan & Norman (1997), both for $\Omega = 1$. The latter simulation is Eulerian, all others are Lagrangian.

are much shallower and the projection effect (illustrated approximately by an arrow in Fig. 8) is small; these profiles are shown without projection. The EMN models are appropriately normalized by the authors using the X-ray emission weighted temperature. ENF report that X-ray temperatures of their simulated clusters are on average equal to the virial temperatures which they use to normalize the profiles. To normalize the KW profile, we use an average X-ray temperature given in Tsai et al. For BN cluster, we calculated the average temperature using the temperature and density profiles.

EMN simulated clusters in $\Omega = 1$ cosmological models with and without inclusion of galactic winds, and in an open model with $\Omega = 0.2$. They also present a flat model (cosmological constant $\Lambda = 1 - \Omega$), which is in general agreement (except in the center) with the better-resolution ENF $\Omega = 0.3$, $\Lambda = 0.7$ simulation, and we show the latter. All these model profiles are in apparent disagreement with our results, being less steep than the observed profiles. The profile for the flat Λ model of ENF only marginally resembles our observations. The EMN $\Omega = 0.2$ model and possibly the ($\Omega = 1 + \text{winds}$) model may have the correct slope at $r > 0.2r_{180}$, but they, too, disagree within the overall range covered by the data. Note, however, that the central regions and the normalizations of the EMN profiles may be considerably incorrect, because their simulations did not resolve cluster cores where a large fraction of the X-ray emission originates. If their simulations underestimate temperatures in the cluster cores because of resolution effects (as is suggested by comparison of their and ENF results for flat Λ models), then

an open model profile may succeed in describing the data.

The no-winds $\Omega = 1$ model of EMN is in disagreement with the observations. However, an independent simulation assuming an $\Omega = 1$ cosmology by KW, who employed the same Lagrangian approach with resolution comparable to EMN, but including radiative cooling, produced a very different temperature profile. The KW profile is in agreement with our observations. A high-resolution Eulerian simulation of an $\Omega = 1$ cluster by BN (which did not include cooling) also produced a steeper temperature profile. KW and BN followed the evolution of only one cluster in each case, and it is unclear to what extent their particular cluster realizations are representative. However, BN report that the dark matter profile of their cluster is well fit by the “universal” profile of Navarro et al. (1997) that fits most simulations with comparable resolution, suggesting that their cluster realization may be close to a typical cluster.

Because the EMN simulations do not reproduce the observed temperature profiles, the $T_X - r_{180}$ relation from EMN that we used to scale the observed profiles may be incorrect. Indeed, the MV97b mass profile measured for A2256 corresponds to an r_{180} a factor of ~ 1.2 smaller than predicted. This means that our temperature data may in fact subtend a larger fraction of r_{180} than shown in Fig. 8. This difference is small and will not qualitatively alter the comparison with models.

We excluded very asymmetric clusters (6 out of 21) in order to obtain a meaningful composite radial profile. In principle, this can bias our comparison with simulations that apparently do not make such a selection. However, as we noted in §6, the excluded cluster profiles are not qualitatively different and would only add scatter to the composite profile. A possibly shallower median slope of the 6 excluded clusters (Fig. 6e) is within the scatter of the profiles shown in Figs. 7 and 8 and therefore will not change any of our conclusions.

The comparison presented above shows that our temperature profile can potentially provide a useful constraint for cluster formation models and, possibly, for the underlying cosmology. At present, however, the disagreement among different simulation techniques is greater than the uncertainty of our measurements. It is also noteworthy that none of the simulations discussed above reproduces the observed shallow gas density profiles (see, e.g., Jones & Forman 1984 for a large sample; Briel, Henry, & Böhringer 1992 and Elbaz, Arnaud, & Böhringer 1995 for data at large cluster radii). A possible exception is the model with galactic winds (Metzler & Evrard 1997, presented in EMN) that predicts a shallow gas profile for cool but not for hot clusters. The temperature and density distributions are related through the hydrostatic equilibrium equation, and if one is not predicted correctly then the other would also be in error, for a given dark matter profile. Therefore, in the short term, our temperature profiles underscore the need to improve the cluster simulations.

7.2.4. The Outliers

Although all but one of the 19 symmetric clusters shown in Figs. 5c and 7 exhibit remarkably similar temperature profiles and the remaining one is still consistent within errors with the common profile, it is interesting to identify the most prominent outliers. The isothermal profile corresponds to A3391 and two other shallow profiles correspond to A399 and A3558. Curiously, all three clusters are located in the regions of high local matter density — A3391 and A399 are members of close pairs and A3558 is in the center of the dense Shapley Supercluster. If

the simulations discussed above capture the qualitative dependence of the profiles on Ω_0 correctly, one would indeed expect to find less steep average temperature profiles in clusters located in relatively overdense regions of the Universe (that is, regions with a high local value of Ω_0).

7.3. A Note of Caution

Finally, we would like to emphasize that the temperature profiles presented here are not direct measurements but result from considerable corrections for the complex scattering of the ASCA mirrors. Therefore, for almost all clusters in our sample, the errors are dominated by the systematic component, mainly due to the uncertainties in the ASCA PSF and effective area. If our current understanding of the ASCA instruments is significantly flawed, the likely result would be that all our temperature profiles become systematically steeper or shallower. Therefore, even though the true individual temperature values should be within our confidence intervals that include conservative estimates for all current uncertainties, the individual profiles shown in Fig. 7 cannot be averaged in any sense, because their errors are not independent.

8. SUMMARY

We systematically analyzed ASCA data for 30 nearby bright clusters and found that none of them is isothermal, excluding those few for which our accuracy is insufficient. Apart from cooling flows, the gas temperature varies with position within each cluster by a factor of 1.3–2 and sometimes stronger. For most clusters, we were able to reconstruct crude two-dimensional gas temperature maps. These maps (together with the images for three clusters without accurate maps) show that half of the clusters in our sample exhibit signs of ongoing merging. In about 60% of the sample, we detect a central cooling flow component.

For all clusters, we obtained radial temperature profiles. Almost all clusters show a temperature decrease with radius (in addition to the central cool components found in many clusters). We excluded the most asymmetric clusters for which a radial profile has no meaning, and compared the normalized temperature profiles for the remaining clusters. While the profiles are different in angular (or ASCA detector) units, when plotted in radial units normalized to the estimated virial radius for each cluster, they are remarkably similar. For a 7 keV cluster with a typical gas density profile, the observed temperature decline can be characterized by a polytropic index of 1.2–1.3, although this is not a particularly good description over the range of measured radii.

The observed temperature decline implies that, at small radii, an analysis that assumes the hydrostatic equilibrium and a constant temperature underestimates the cluster mass, while at large radii, the gravitating mass falls below the isothermal estimate. In particular, for a 7 keV cluster with our median temperature profile and a typical gas density distribution, the total mass estimates within 0.15 and $0.9 h^{-1}$ Mpc are approximately factors of 1.35 and 0.7 above and below the isothermal β -model estimates, respectively. As discussed in the study of A2256 (MV97b), this general result strengthens the argument for a low- Ω_0 cosmology based on the high baryon fraction in clusters (e.g., White et al. 1993). It also implies a strong segregation of gas and dark matter, possibly indicating that sources other than gravity have produced a significant fraction of the gas thermal energy (e.g., David et al. 1995).

Finally, we compared our composite temperature profile to the results of cluster hydrodynamic simulations. We find that most simulations predict a considerably shallower average radial temperature decline, with the possible exception of those for low- Ω cosmologies. This comparison suggests that, potentially, the ASCA temperature profiles can constrain cluster formation models. However, at present, there is a discrepancy between different simulations that is greater than the uncertainty in our measurements. This underscores the need for further theoretical and numerical work before conclusions can be drawn regarding which cosmological parameters best describe the observations.

The results reported here would not be possible without the dedicated work of the entire ASCA team on building, calibration and operation of the observatory. We thank NASA/GSFC for maintaining the HEASARC online data archive which we used extensively. We are grateful to Franz Bauer for sharing his results prior to publication, and to Ue-Li Pen, Nancy Brickhouse and the anonymous referee for useful comments. M. M. and W. R. F. acknowledge support from Smithsonian Institution, NASA grant NAG5-2611, and NASA contract NAS8-39073. C. L. S. was supported in part by NASA grants NAG5-2526 and NAG5-4516. A. V. was supported by CfA postdoctoral fellowship.

REFERENCES

- ABC Guide, <http://heasarc.gsfc.nasa.gov/docs/asca/abc/abc.html>
- Allen, S. W. 1998, MNRAS, submitted; astro-ph/9710217
- Bahcall, J. N., & Sarazin, C. L. 1977, ApJ, 213, L99
- Bauer, F., & Sarazin, C. L. 1998, in preparation
- Bertschinger, E. 1985, ApJS, 58, 39
- Briel, U. G., et al. 1991, A&A, 246, L10
- Briel, U. G., Henry, J. P., & Böhringer, H. 1992, A&A, 259, L31
- Briel, U. G., & Henry, J. P. 1994, Nature, 372, 439
- Briel, U. G., & Henry, J. P. 1996, ApJ, 472, 131
- Bryan, G. L., & Norman, M. L. 1997, in Computational Astrophysics, Proc. 12th Kingston Conference, eds. D. Clarke & M. West (PASP), astro-ph/9710186 (BN)
- Buote, D. A., & Tsai, J. C. 1996, ApJ, 458, 27
- David, L., Jones, C., & Forman, W. 1995, ApJ, 445, 578
- David, L., Slyz, A., Jones, C., Forman, W., Vrtilik, S. D., & Arnaud, K. A. 1993, ApJ, 412, 479
- Dickey, J. M., & Lockman, F. J. 1990, ARA&A, 28, 215
- Donnelly, R. H., Markevitch, M., Forman, W., Jones, C., Churazov, E., Gilfanov, M., & David, L. P. 1997, ApJ, submitted
- Dotani, T., Yamashita, A., Rasmussen, A., & the SIS team, 1995, ASCA Newsletter, # 3 (NASA/GSFC)
- Durret, F., Forman, W., Gerbal, D., Jones, C., & Vikhlinin, A. 1997, A&A, to be submitted
- Ebeling, H., Voges, W., Böhringer, H., Edge, A. C., Huchra, J. P., & Briel, U. G. 1996, MNRAS, 281, 799
- Edge, A. C., & Stewart, G. C. 1991, MNRAS, 252, 414
- Edge, A. C., & Stewart, G. C., & Fabian, A. C. 1992, MNRAS, 258, 177
- Eke, V. R., Navarro, J. F., & Frenk, C. S. 1997, ApJ, submitted; astro-ph/9708070 (ENF)
- Evrard, A. E., Metzler, C. A., & Navarro, J. F. 1996, ApJ, 469, 494 (EMN)
- Eyles, C. J., Watt, M. P., Bertram, D., Church, M. J., & Ponman, T. J. 1991, ApJ, 376, 23
- Ezawa, H., Fukazawa, Y., Makishima, K., Ohashi, T., Takahara, F., Xu, H., & Yamasaki, N. 1997, ApJ, 490, L33
- Fabian, A. C. 1994, ARA&A, 32, 227
- Fabian, A. C., Arnaud, K. A., Bautz, M. W., & Tawara, Y. 1994a, ApJ, 436, L63
- Fabian, A. C., Crawford, C. S., Edge, A. C., & Mushotzky, R. F. 1994b, MNRAS, 267, 779
- Fabian, A. C., Peres, C. B., & White, D. A. 1997, MNRAS, 285, L35
- Frenk, C. S., et al. 1998, in preparation
- Fujita, Y., Koyama, K., Tsuru, T., & Matsumoto, H. 1996, PASJ, 48, 191
- Gendreau, K., & Yaqoob, T. 1997, ASCA Newsletter, # 5 (NASA/GSFC)
- Gotthelf, E. 1996, ASCA Newsletter, # 4 (NASA/GSFC)
- Hatsukade, I. 1989, Ph.D. thesis, Osaka Univ.
- Henriksen, M., & Markevitch, M. 1996, ApJ, 466, L79
- Henriksen, M. J., & White, R. E. 1996, ApJ, 465, 515
- Henry, J. P., & Briel, U. G. 1995, ApJ, 443, L9
- Henry, J. P., & Briel, U. G. 1996, ApJ, 472, 137
- Honda, H., et al. 1996, ApJ, 473, L71
- Huang, Z., & Sarazin, C. L. 1998, ApJ, 496, in press
- Hughes, J. P., Gorenstein, P., & Fabricant, D. 1988, ApJ, 329, 82
- Ikebe, Y., et al. 1996, Nature, 379, 427
- Ikebe, Y., et al. 1997, ApJ, 481, 660
- Ishisaki, Y., 1996, PhD thesis, University of Tokyo
- Jones, C., Donnelly, H., Forman, W., Markevitch, M., Vikhlinin, A., Churazov, E., & Gilfanov, M. 1997, in Untangling Coma Berenices, Marseilles, ed. A. Mazure (World Scientific), in press
- Jones, C., & Forman, W. 1984, ApJ, 276, 38
- Jones, C., & Forman, W. 1997, ApJS, submitted
- Katz, N., & White, S. D. M. 1993, ApJ, 412, 455 (KW)
- Kellogg, E. M., Gursky, H., Tananbaum, H., Giacconi, R., & Pounds, K. 1972, 174, L65
- Koyama, K., Takano, S., & Tawara, Y. 1991, Nature, 350, 135
- Lacey, C., & Cole, S. 1993, MNRAS, 262, 627
- Loewenstein, M. 1997, in X-ray Imaging and Spectroscopy of Cosmic Plasmas, ed. F. Makino (Tokyo: Universal Academy), 67
- Makishima, K. 1996, ASCA calibration memo
- Markevitch, M. 1996, ApJ, 465, L1 (M96)
- Markevitch, M., et al. 1998, in preparation (M98)
- Markevitch, M. 1998, ApJ, submitted (astro-ph/9802059)
- Markevitch, M., Mushotzky, R. F., Inoue, H., Yamashita, K., Furuzawa, A., & Tawara, Y. 1996a, ApJ, 456, 437
- Markevitch, M., Sarazin, C. L., & Irwin, J. A. 1996b, ApJ, 472, L17 (MSI)
- Markevitch, M., & Vikhlinin, A. 1997a, ApJ, 474, 84 (MV97a)
- Markevitch, M., & Vikhlinin, A. 1997b, ApJ, 491, 467 (MV97b)
- Markevitch, M., Yamashita, K., Furuzawa, A., & Tawara, Y. 1994, ApJ, 436, L71
- Mathews, W. G. 1978, ApJ, 219, 413
- Metzler, C. A., & Evrard, A. E. 1997, ApJ, submitted (astro-ph/9710324)
- Miralda-Escudé, J., & Babul, A. 1995, ApJ, 449, 18
- Mitchell, R., Culhane, J., Davison, P., & Ives, J. 1976, MNRAS, 189, 329
- Navarro, J. F., Frenk, C. S., & White, S. D. M. 1997, ApJ in press
- Owen, F. N., Ledlow, M. J., Morrison, G. E., & Hill, J. M. 1997, ApJ Letters, in press (astro-ph/9708150)
- Ponman, T. J., & Bertram, D. 1993, Nature, 363, 51
- Press, W. H., Teukolsky, S. A., Vetterling, W. T., & Flannery, B. P. 1992, Numerical Recipes (Cambridge University Press)
- Reynolds, C. S., & Fabian, A. C. 1996, MNRAS, 278, 479
- Richstone, D., Loeb, A., & Turner, E. L. 1992, ApJ, 393, 477
- Roettiger, K., Burns, J., & Loken, C. 1993, ApJ, 407, L53
- Sarazin, C. L. 1988, X-ray Emission from Clusters of Galaxies (Cambridge: Cambridge University Press)
- Sarazin, C. L., & Graney, C. M. 1991, ApJ, 375, 532
- Sarazin, C. L., & McNamara, B. R. 1997, ApJ, 480, 203
- Sarazin, C. L., Wise, M. W., & Markevitch, M. L. 1997, ApJ, submitted
- Schindler, S., & Müller, E. 1993, A&A, 272, 137
- Serlemitsos, P. J., et al. 1995, PASJ, 47, 105
- Snowden, S. L., McCammon, D., Burrows, D. N., & Mendenhall, J. A. 1994, ApJ, 424, 714
- Soltan A. J., Hasinger, G., Egger, R., Snowden, S., & Trümper, J. 1996, A&A, 305, 17
- Takahashi, T., Markevitch, M., Fukazawa, Y., Ikebe, Y., Ishisaki, Y., Kikuchi, K., Makishima, K., & Tawara, Y. 1995, ASCA Newsletter, # 3 (NASA/GSFC)
- Tanaka, Y., Inoue, H., & Holt, S. S. 1994, PASJ, 46, L37
- Thomas, P. A., et al. 1997, MNRAS, submitted (astro-ph/9707018)
- Tsai, J. C., & Buote, D. A. 1996, MNRAS, 282, 77
- Tsai, J. C., Katz, N., & Bertschinger, E. 1994, ApJ, 423, 553
- Ueno, S. 1996, PhD thesis, University of Tokyo
- Ueno, S., Koyama, K., Nishida, M., Yamauchi, S., & Ward, M. J. 1994, ApJ, 431, L1
- Vikhlinin, A., & Forman, W. 1995, ApJ, 455, L109
- Watt, M. P., Ponman, T. J., Bertram, D., Eyles, C. J., Skinner, G. K., & Willmore, A. P. 1992, MNRAS, 258, 738
- Way, M. J., Quintana, H., & Infante, L. 1997, ApJ, submitted (astro-ph/9709036)
- White, D. A., Fabian, A. C., Allen, S. W., Edge, A. C., Crawford, C. S., Johnstone, R. M., Stewart, G. C., & Voges, W. 1994, MNRAS, 269, 589
- White, S. D. M., Navarro, J. F., Evrard, A. E., & Frenk, C. S. 1993, Nature, 366, 429
- White, S. D. M., & Rees, M. J. 1978, MNRAS, 183, 341